



Quantitative Susceptibility Mapping using Echo Planar Imaging

DIPLOMARBEIT

zur Erlangung des akademischen Grades

Diplom-Ingenieur

im Rahmen des Studiums

Biomedical Engineering

eingereicht von

Beáta Bachratá

Matrikelnummer 1528777

an der Fakultät für Physik

der Technischen Universität Wien

Betreuung: **Univ.Prof. Dipl. -Ing. Dr.techn. Gerald Badurek**

Assoc.Prof. Dr. Simon Robinson

Wien, 14. Juni 2017

Beáta Bachratá

Gerald Badurek



TECHNISCHE
UNIVERSITÄT
WIEN
Vienna University of Technology

Quantitative Susceptibility Mapping using Echo Planar Imaging

MASTER THESIS

submitted in partial fulfillment of the requirement for the degree of

Master of Science

in

Biomedical Engineering

by

Beáta Bachratá

Registration number 1528777

to the Faculty of Physics

at the Vienna University of Technology

Supervised by: **Univ.Prof. Dipl. -Ing. Dr.techn. Gerald Badurek**

Assoc.Prof. Dr. Simon Robinson

Vienna, 14. June 2017

Beáta Bachratá

Gerald Badurek

Erklärung zur Verfassung der Arbeit

Beáta Bachratá,
Jégého 8, 82108 Bratislava, Slovakia

Hiermit erkläre ich, dass ich diese Arbeit selbstständig verfasst habe, dass ich die verwendeten Quellen und Hilfsmittel vollständig angegeben habe und dass ich die Stellen der Arbeit – einschließlich Tabellen, Karten und Abbildungen –, auf anderen Werken oder dem Internet im Wortlaut oder dem Sinn nach entnommen sind, auf jeden Fall unter Angabe der Quelle als Entlehnung kenntlich gemacht habe.

Wien, 14. Juni 2017

Beáta Bachratá

Acknowledgements

At this point I would like to thank to everybody who supported me during the course of the work on this thesis. First and foremost, I would like to thank to my supervisor from the Medical University of Vienna, Simon Robinson, for the opportunity to work on such an interesting project and for the very enthusiastic and expert guidance of my thesis. I also want to thank Karin Poljanc and Gerald Badurek for supervising my thesis at the Vienna University of Technology.

A special thanks goes to Korbinian Eckstein, for introducing me to the ICE programming. Furthermore I want to thank Pedro Cardoso for all the technical support and for creating very nice working atmosphere.

Abstract

Quantitative Susceptibility Mapping (QSM) is a postprocessing Magnetic Resonance Imaging (MRI) technique that provides contrast based on the magnetic susceptibility of the object. Since QSM is very sensitive to iron, calcium, gadolinium and myelin, it can be used to characterize microbleeds, investigate demyelination, quantify iron content in deep grey matter structures and visualise vessels. Due to the long acquisition time (up to 10 min.) of the high resolution gradient-echo (GRE) scans which are conventionally used to acquire the T_2^* -weighted scans which are sensitive to susceptibility, this method is very prone to motion, limiting its clinical applicability.

The Echo-Planar Imaging (EPI) sequence can acquire images with the same volumetric coverage within a fraction of the time (usually few seconds), thereby it is less vulnerable to motion. In EPI the signal is usually collected for the large part of imaging time (around 75%), leading to a very high efficiency. Moreover, since the whole k-space can be sampled after a single excitation pulse, the full longitudinal magnetization may be available for the image formation. Because the speed of physiological processes and the EPI's imaging speed are similar, the sequential acquisition of EPI scans, functional MRI (fMRI), allows for observation of physiological fluctuations. Since in some patient groups (e.g. patients with Alzheimer, Multiple sclerosis, Parkinson) the fMRI is done to investigate functional impairment, this data could be used also for QSM analysis, enabling both functional information and semi-quantitative structural information to be derived from the same scan.

QSM analysis uses the usually discarded phase of the complex MR signal, which is proportional to the local deviation from the static magnetic field and hence dependent on the magnetic susceptibility of the tissue. Since nowadays the signal is usually acquired by the array of radio-frequency coils each having its own, spatially varying phase offset, the difficult combination of phases from contributing coils is required. This gets even more complicated in the EPI, due to its inherent higher noise content.

In this project, we establish the methodological steps necessary to use 7 T task or resting state fMRI data to perform QSM, without the need to acquire any additional data. To achieve that, a number of variants of a phase combination methods called the Virtual Receiver Coil (VRC) approach were proposed and assessed. These were shown to achieve high-quality combination even for quite low-quality EPI data, with different variants having different characteristics and some suffering from artifacts. Phase combination was implemented in the Siemens Image Reconstruction Environment to run on the MR scanner. The combined phase EPI data was used for QSM analysis and the susceptibility maps

were compared with those from a reference GRE measurement. Further the effects of motion and physiological fluctuations on the QSM results were studied by the functional QSM analysis.

We have shown that although the QSM analysis using EPI is feasible, to obtain the results comparable to those of GRE data at least the higher resolution acquisition is required. However, there are still many other differences compared to GRE (e.g. EPI inherent phase corrections, echo time variability across k-space, additional phase shifts in parallel imaging, signal dropouts, etc.) whose effects on QSM analysis need to be addressed, before the EPI data could be use with the same reliability as GRE data. Further we have shown that to observe the task related and physiological fluctuation related changes in the QSM analysis of fMRI time-series, the higher resolution and the application of additional preprocessing steps are necessary.

Kurzfassung (Abstract)

Quantitative Suszeptibilitätskartierung (QSM) ist ein Nachbearbeitungsverfahren der Magnetresonanztomographie (MRT), welches die Suszeptibilitätsverteilung des gemessenen Objekts berechnet. Wegen der hohen Sensitivität auf Eisen, Gadolinium und Myelin wird QSM dazu benutzt Mikroblutungen zu charakterisieren, Demyelinisierungen zu untersuchen, den Eisengehalt der Strukturen in tiefer grauer Substanz zu bestimmen und auch um Gefäße sichtbar zu machen. Konventionell werden hochauflösende, T_2^* -gewichtete Gradientenechosequenzen (GRE) verwendet, die eine hohe Sensitivität auf die Suszeptibilität aufweisen, jedoch aufgrund der sehr langen Aufnahmezeit (bis zu 10 min.) anfällig für Bewegungsartefakte sind, was die klinische Anwendbarkeit einschränkt.

Mit dem Echo-Planar Verfahren (EPI) kann dasselbe Volumen in einem Bruchteil der Zeit (üblicherweise in wenigen Sekunden) aufgenommen werden, was die Gefahr durch Bewegung während der Aufnahme deutlich reduziert. EPI-Sequenzen sind sehr effizient, da sie den gesamten k-Raum nach einem einzigen Anregungspuls abrastern können, wobei sie zum einen die volle longitudinale Magnetisierung nutzen können und zum anderen auch den Großteil der Messzeit mit der tatsächlichen Datenaufnahme verbringen (ca. 75%). Da die Zeitspanne einer EPI-Aufnahme und physiologischer Prozesse vergleichbar ist, ermöglicht eine sequentielle Aufnahme von EPI-Bildern die Erfassung physiologischer Schwankungen, was als funktionelle MRT (fMRT) bezeichnet wird. Da zur Erkennung von funktionalen Störungen fMRT-Messungen routinemäßig an Patienten mit Krankheiten wie Alzheimer, multipler Sklerose oder Parkinson durchgeführt werden, könnten dieselben Aufnahmen auch zur Berechnung von QSM verwendet werden um aus einer Messung sowohl funktionelle als auch semi-quantitative strukturelle Informationen zu erhalten.

Für die Berechnung von QSM wird die gewöhnlich außer Acht gelassene Phaseninformation des komplexwertigen MR-Signals verwendet, welche proportional zur lokalen Abweichung des statischen Magnetfeldes ist und somit von der Suszeptibilität des Gewebes abhängt. Da das MR-Signal heutzutage meist von einem Spulen-Array aufgenommen wird, ist es nötig ein kombiniertes Phasenbild zu berechnen, was jedoch schwierig ist, da jede Spule eine eigene örtlich variierende Phasenverschiebung aufweist. Bei EPI-Aufnahmen ist die Spulenkombination sogar nochmals schwieriger, da diese einen höheren Rauschanteil aufweisen.

In diesem Projekt ermitteln wir die methodologischen Schritte, die nötig sind um QSM von aufgabenbezogenem oder Ruhezustands-fMRI ohne zusätzliche Messungen zu berechnen. Um dieses Ziel zu erreichen wurden verschiedene

Varianten der Phasenkombinationsmethode Virtual Receiver Coil (VRC) entwickelt und getestet. Es wurde gezeigt, dass alle Varianten sogar für niedrigqualitative EPI-Daten eine hohe Kombinationsqualität erreichen, wobei die Varianten unterschiedliche Eigenschaften aufweisen und manche artefaktbehaftet sind. Die Phasenkombination wurde in der Siemens Image Reconstruction Environment implementiert und ist wird auf dem MR Scanner berechnet. Die kombinierten EPI-Phaseninformationen wurden für die Berechnung von QSM benutzt und die erhalten Suszeptibilitätskarten wurden mit jenen verglichen die von einer GRE-Referenzmessung berechnet wurden. Zusätzlich wurden noch die durch Bewegung und physiologisch bedingte Schwankungen hervorgerufenen Effekte auf die QSM-Ergebnisse mittels funktioneller QSM analysiert.

Wir haben gezeigt, dass, obwohl QSM-Berechnungen auf EPI Daten möglich sind, trotzdem zumindest höheraufgelöste Messungen benötigt werden, um mit GRE-Daten vergleichbare Ergebnisse zu erhalten. Es gibt jedoch viele weitere Unterschiede zu GRE (z.B. inhärente Phasenkorrektur bei EPI, Variabilität der Echozeit im k-Raum, zusätzliche Phasenverschiebungen aufgrund von paralleler Bildgebung, lokalen Signalauslöschungen, etc.), deren Effekte auf die QSM-Berechnung adressiert werden müssen, bevor EPI-Daten mit derselben Verlässlichkeit wie GRE-Daten verwendet werden können. Außerdem haben wir gezeigt, dass höhere Auflösung und die Anwendung zusätzlicher Vorverarbeitungsschritte nötig sind um die aufgabenbezogenen und die aufgrund physiologischer Schwankungen hervorgerufenen Änderungen in QSM aus fMRI-Zeitserien zu beobachten.

List of Abbreviations

AC	Adaptive Combine
ASPIRE	A Simple Phase Image Reconstruction for multi-echo acquisitions (a method for combining phase data from multi-channel coils)
BOLD	Blood-oxygenation-level dependent
CBF	Cerebral blood flow
CBV	Cerebral blood volume
CMRO₂	Cerebral metabolic rate of oxygen
COMPOSER	Combining phased array data using offsets from a short echo-time reference (a method for combining phase data from multi-channel coils)
deoxyHb	Deoxygenated hemoglobin
EPI	Echo-planar imaging
FA	Flip angle
FE	Frequency-encoding
FID	Free induction decay
fMRI	Functional MRI
fQSM	Functional QSM
GLM	General Linear Model
GRAPPA	Generalized Autocalibrating Partially Parallel Acquisition
GRE	Gradient-echo
HiP	Hermitian Inner Product
ICA	Independent Component Analysis
ICE	Image Calculation Environment
MB	Multiband
MCPC-3D-I	Multi-channel phase combination using 3D phase offsets derived from a dual echo scan (first variant)
MCPC-3D-II	Multi-channel phase combination using 3D phase offsets derived from a dual echo scan (second variant)
MRI	Magnetic Resonance Imaging

mwSPM	Magnitude-weighted SPM
NR	Number of repetitions
oxyHb	Oxygenated hemoglobin
PE	Phase-encoding
PF	Partial Fourier
PI	Parallel Imaging
PICA	Probabilistic Independent Component Analysis
QSM	Quantitative susceptibility mapping
rBW	Receiver bandwidth
RF	Radiofrequency
ROI_M	Matching region of interest
SE	Spin-echo
SENSE	Sensitivity Encoding
SMS	Simultaneous Multi-slice
SNR	Signal-to-noise ratio
SPM	Scalar Phase Matching
tBW	Transceiver bandwidth
TE	Echo time
TGV	Total Generalized Variation
TR	Repetition time
tSNR	Time-series SNR
UHF	Ultra-high field
VBC	Virtual Body Coil
VRC	Virtual Reference Coil

Table of Contents

1	INTRODUCTION	1
1.1	Motivation and related work	1
1.2	Aim	3
2	THEORY	4
2.1	Principles of Magnetic Resonance Imaging	4
2.1.1	Magnetic spin	4
2.1.2	Macroscopic magnetization	5
2.1.3	Radiofrequency excitation	6
2.1.4	Relaxation	7
2.1.5	Image creation	8
2.1.6	Gradient-echo sequence	10
2.1.7	Ultra-high field MRI	12
2.2	MRI phase signal	12
2.2.1	Unwrapping	13
2.2.2	Phase problems (open-ended fringelines)	15
2.2.3	Principles of phase combination	15
2.2.4	Phase combination methods	17
2.2.5	Virtual Reference Coil method	21
2.3	Quantitative Susceptibility Mapping	24
2.3.1	Estimation of the magnetic field distribution	25
2.3.2	Background field removal	25
2.3.3	Dipole inversion	26
2.3.4	Total Generalized Variation based QSM algorithm	28
2.4	Functional Magnetic Resonance Imaging	29
2.4.1	Blood-oxygenation-level dependent contrast	29
2.4.2	Echo-planar imaging sequence	31
2.4.3	Nyquist ghost correction	35
2.4.4	Statistical analysis	36
3	METHODS	39
3.1	Data acquisition	39
3.2	VRC implementation	41
3.2.1	Offline (in MATLAB)	41
3.2.2	Online (in the Siemens Image Calculation Environment)	42
4	ANALYSIS	44

4.1	Evaluation of VRC combination	44
4.2	fMRI analysis	44
4.3	QSM analysis	44
5	RESULTS	47
5.1	VRC performance	47
5.2	fMRI analysis	53
5.3	QSM analysis	54
6	DISCUSSION	60
7	CONCLUSION	64
	REFERENCES	65

1 Introduction

1.1 Motivation and related work

Conventionally, fMRI and QSM have been performed using two sets of separately acquired images; a rapid series of quite low resolution echo-planar imaging data for fMRI, and a high resolution gradient-echo 3D scan for QSM. However, the high resolution of GRE comes at the price of acquisition time (circa 5-10 min) and so of a higher sensitivity to motion. Beside the presence of susceptibility sources like iron and myelin that are constant in time (on the measurement timescale), the GRE QSM results may be also influenced by the susceptibility sources that depend on the physiological fluctuations, blood flow and the oxygenation level changes [1] and thereby vary in time.

Echo-planar imaging [2] is fast sequence, usually based on GRE technique, which is sensitive to local field inhomogeneities and therefore also to the susceptibility distribution. It uses oscillating readout gradient to acquire a signal from the whole k-space of a certain slice after application of single excitation pulse. In the past, the EPI's resolution, dependent on the maximum gradient amplitude-time product, was quite low, as its increase by prolonging gradient pulses would enhance the geometrical distortions and signal dropouts. However, thanks to the recent development of techniques like partial Fourier or Parallel Imaging, the acquisition of high resolution EPI within a few seconds is possible. Since EPI data also contain phase information, they can be used for much more rapid generation of QSMs. The feasibility of using conventional single-shot 2D EPI for QSM reconstruction within a few seconds was demonstrated by Sun and Wilman [3]. They also showed that although EPI is more sensitive to gradient performance, chemical shift effects and bias fields, it yields very similar susceptibilities to those of "gold standard" GRE. Bilgic et al. [4] demonstrated the possibility of using multiband accelerated 2D EPI acquisition for QSM and the benefits of using wave-CAIPI, which achieves high acceleration with low artifact and noise amplification penalties, for the QSM reconstruction. Due to the substantial SNR benefits of 3D acquisitions for high resolution whole-brain imaging, Langkammer et al. [5] proposed to use 3D EPI sequence in combination with TGV-based QSM algorithm, to yield reliable, high resolution QSM images in about a minute by averaging QSMs obtained from several EPI scans. In all of these studies, the data for EPI-based QSMs were acquired explicitly for that purpose.

If the functional time-series is measured, the QSM analysis can be carried on each volume separately, generating time-series of QSMs. Then the average QSM with decreased noise levels can be generated or the susceptibility changes caused

by BOLD effect can be observed and quantitatively assessed, i.e. the so-called functional QSM (fQSM) [6] analysis can be performed. Since the susceptibility depends less strongly on the field strength [7] and on acquisition sequence and its parameters [8], the better reproducibility and a more direct relation to the physiology than in fMRI could be reached. Due to the removal of non-local signal contributors inherent to QSM processing, the functional QSM also allows for the more precise localization of neuronal activation than fMRI, however for the price of decreased signal intensity. Further, it has been shown that the fQSM is more likely to be affected by activation unrelated physiological changes than the general fMRI [9][10].

The generation of QSMs directly from task or resting state fMRI data was recently demonstrated [4] [11] [12] [13]. In these studies, the activation maps as well as the structural, iron-sensitive QSMs were retrieved from the same EPI task time-series and the following functional analysis of magnitude and QSM timeseries was performed. Biancardi et al. [13] showed, that the BOLD related QSM changes in both, activated area and corresponding large draining veins, can be detected and that they are induced by the blood volume and oxygenation changes. Similarly, Ozbay et al. showed a good correlation between fQSM and fMRI signal timecourses. Additionally they observed that the fQSM besides enabling for better localization of large-vessel BOLD effects, it is capable of detecting activation even in tissues without larger vessels. However, as demonstrated by Balla et al. [6], the fQSM's sensitivity and spatial reliability (relative to fMRI) strongly depends on the applied spatio-temporal filtering and on the arbitrary setting of significance threshold in SPM. Further, as observed by Sun et al. [11], the fQSM results are more prone to residual background fields and show less functional changes compared to standard magnitude fMRI.

The functional QSM analysis was firstly demonstrated in the studies by Balla et al. [6] at 7 T and by Biancardi et al [13] at 9.4 T, in which thanks to the presence of birdcage transceive part of the head coil, the Roemer methods for combining of phase images from the contributing radio-frequency coils could be used. Beside the fact that the reference coil is often not available and therefore the possibility of using this method is quite restricted, it is also very sensitivity to motion between the reference scan and the main scan. In the studies by Sun et al. [11] and Ozbay et al. [12] at 1.5 T, 3 T and 4.7 T, the less robust reference free phase combination methods (e.g. adaptive combine) were used, which often fail at higher field strengths.

For the reference-free case at field strengths of 7 T or higher, the generation QSMs directly out of EPI task-series has not been yet demonstrated, due to the difficulty in phase combination of single-echo data. Although offline implementations of combination methods that could be use for EPI data exists,

the huge amount of the single-channel data acquired during conventional measurement (~5-10 GB for one run) that would need to be exported, makes this analysis unfeasible. This raises the need for online implementation of robust reference-free single-echo phase combination method. As the best candidate for our requirements, the Virtual Reference Coil (VRC) method was assessed, which can achieve high combination quality, however which does not remove the real phase offsets but rather substitutes them by the phase of created reference coil. As the reference coil may or may not have homogeneous B_1 , the residual non- B_0 -related phase that may influence subsequent analysis if not taken into account. Nevertheless, since no reference scan is required, it is less prone to coregistration errors and therefore motion, which is often problematic in patient cohorts. Furthermore, VRC does not require unwrapping what makes its computational demands quite low, and thereby can be used for online phase combination.

1.2 Aim

The aim of this study was to explore the possibility of generating QSMs directly from the phase of fMRI task or resting state data using variants of an existing phase combination method [14] and to observe the challenges and relative merits of using conventional 2D EPI, 2D simultaneous-multi-slice EPI and 3D EPI instead of the conventionally used GRE.

To achieve the required high-quality phase combination of the EPI data an additional aim was defined, including the determination of the most suitable Virtual Receiver Coil image for the VRC phase combination and the implementation of the VRC approach in the Siemens Image Reconstruction Environment (ICE).

2 Theory

2.1 Principles of Magnetic Resonance Imaging

In Magnetic Resonance Imaging (MRI) not all nuclei can be detected. Only those with both magnetic and angular moments different from zero can be used for signal creation. Furthermore, the fact that only very small part of nuclear magnetic moments contributes to the measured signal, as described by Boltzmann statistics (see Section 2.1.2), is responsible for the very low sensitivity of MRI. The very high biological abundance and spin equal to $+1/2$ therefore make the hydrogen the most often choice for MR imaging, however other nuclei, like phosphorus or sodium can be imaged as well, but with lower sensitivity. In the next chapter we will focus on the properties a single proton.

2.1.1 Magnetic spin

According to quantum mechanics, all particles have inherent property, called spin quantum number (I), which only take non-negative integer or half-integer values:

$$I = 0, \frac{1}{2}, 1, \frac{3}{2}, 2, \dots \quad (1)$$

Particles with integer value of spin are called bosons, while those with half-integer value are called fermions. Unpaired protons, neutrons and electrons have spin equal to $+1/2$. However, when they pair, their spins are summed and atoms with different net values of spin are created.

When a thermodynamic temperature of a nuclei is different from 0 K, the thermal energy forces them to quickly rotate around their axis. As they are positively charged and have non-zero mass, this motion creates an angular moment (\mathbf{L}) and a small magnetic field known as magnetic moment ($\boldsymbol{\mu}$). The angular moment, often referred as spin, is given as

$$\mathbf{L} = \boldsymbol{\omega} m r^2, \quad (2)$$

where $\boldsymbol{\omega}$ represents the angular frequency and r the radius of the rotational motion. It can be also defined by using spin quantum number

$$|\mathbf{L}| = \sqrt{\hbar(I(I+1))}, \quad (3)$$

where \hbar denotes reduced Planck constant. This equation depicts, that the spin is also quantized.

The magnitude of the magnetic moment is defined as the ratio between the maximum torque created by external field on a rotating particle (τ_{max}) and the external field strength (B_0)

$$\mu = \frac{\tau_{max}}{B_0}, \quad (4)$$

and the orientation is given by right hand rule.

Their ratio, called gyromagnetic ratio, is constant for each nucleus regardless of the field strength or temperature, which can be written as

$$\gamma = \frac{\mu}{L} = \frac{q}{2m}, \quad (5)$$

with q denoting the charge and m the mass of the nuclei.

2.1.2 Macroscopic magnetization

The magnetic energy (E_{mag}) of a nucleus depends on the interaction between its magnetic moment and external magnetic field \mathbf{B}_0 , in which it is placed:

$$E_{mag} = -\mu \cdot \mathbf{B}_0, \quad (6)$$

and reaches its minimum, when they are oriented parallelly.

If no external magnetic field is present, the orientations of angular moments of spins (spins polarization axis) are random. In a sufficiently large sample, all orientations of angular moments are equally represented, resulting in the net cancelation of magnetic moments of spins. The total magnetic moment of the sample is then very closed to zero.

When the sample is placed in external magnetic field, as spins pose both angular and magnetic moment, they start to precess around \mathbf{B}_0 with the so-called Larmor frequency given by

$$\omega = -\gamma B_0. \quad (7)$$

During this precession motion, the magnetic moment of a spin moves on a conical surface. The angle between the magnetic moment and the field depends on the initial spin polarization and is kept constant, if no other fields are present.

However, the field perceived by each spin is given by the sum of the static external field and the very small time-varying field, created by the motion of the surrounding magnetic particles. Therefore, the total magnetic field seen by each spin is slightly different and varying in time, since due to the thermal energy the Brownian motion of particles occurs. These small fluctuations are responsible for very slow changes of the precession cone angles. And because this reorientational motion is driven by the thermal energy, it is biased towards the lower energy state, where magnetic moment of spin is parallel with \mathbf{B}_0 . After certain time, the system reaches a stable state with anisotropic distribution of spins orientations, referred as thermal equilibrium [15].

To calculate the equilibrium magnetization (net magnetic moment), the simplification where all spins are projected to only two eigenstates, lower energy

parallel (\uparrow) and higher energy antiparallel (\downarrow), can be used [16]. The energy difference (ΔE) of these two states is defined by Zeeman effect

$$\Delta E = \hbar\gamma B_0, \quad (8)$$

and together with the thermodynamic temperature T determines the distribution of spins into them as described by Boltzmann statistics

$$\frac{N_\uparrow}{N_\downarrow} = \exp\left(\frac{\Delta E}{kT}\right) = \exp\left(\frac{\hbar\gamma B_0}{kT}\right) = \exp\left(\frac{-\hbar(\omega_\uparrow - \omega_\downarrow)}{kT}\right), \quad (9)$$

where k represents Boltzmann constant.

Because of this population difference of spins in a system at thermal equilibrium, the macroscopic magnetization (\mathbf{M}_0) is created. Its magnitude, given by Curie's law

$$M_0 = \frac{(N_\uparrow - N_\downarrow)\gamma h^2 I(I + 1)}{3kT}, \quad (10)$$

remains the same, unless the temperature of the system changes. Nevertheless, as the magnetization distribution of spins is symmetrical around the z -axis, there is no transverse magnetization (\mathbf{M}_{xy}) (in xy -plane component) and only the longitudinal magnetization (\mathbf{M}_z) exists. The total magnetization is therefore aligned parallelly to \mathbf{B}_0 , and because it is very small compared to the B_0 it cannot be measured easily. For imaging, the transversal component has to be created, by using radiofrequency (RF) excitation.

2.1.3 Radiofrequency excitation

When additional electromagnetic field \mathbf{B} (RF-pulse) oscillating with Larmor frequency of observed spin system is applied, the transverse magnetization is created by simultaneous action of two distinct processes.

Firstly, the energy of the RF-pulse is absorbed, resulting in the system's energy increase. The reorientational motion of spins is therefore getting less biased towards the lower energy state and the longitudinal magnetization decreases. Secondly, the RF-pulse application synchronizes precession phases of all spins, so leads to the creation of the transverse magnetization. The \mathbf{M}_{xy} then rotates around the z -axis with Larmor frequency. As these effects require the frequency of RF pulse and precession frequency of spins to be equal, i.e. in resonance, they are both together often referred as resonance [17].

To make the description of the magnetization vector's evolution easier, the rotating frame of reference is defined, which rotates around the z -axis with the Larmor frequency. Here, the RF-pulse application leads to a simple tilting of the net magnetization vector by a certain angle, which is determined by pulse amplitude and duration and often referred as flip angle (FA). RF-pulse triggering symmetrical redistribution of spins' magnetizations around xy -plane is known as

90° pulse, since it tilts the magnetization vector into the transverse plane. If the same RF-pulse would be applied for a longer duration, the reorientation of spins towards the higher energy state would occur and the magnetization vector would be tilted by a larger angle. The pulse causing the inversion of initial longitudinal magnetization is known as a 180° pulse.

2.1.4 Relaxation

When the application of RF-pulse is ended, two simultaneous processes trigger the return of the spin system back to the state of thermal equilibrium. These processes are known as a relaxation.

Firstly, due to the energy transfer to the surrounding (lattice), the reorientational motion of spins gets again more biased towards the lower energy - parallel state. The longitudinal magnetization of thermal equilibrium (\mathbf{M}_0) is thus getting slowly restored. This process is called longitudinal or spin-lattice relaxation and can be described as

$$\mathbf{M}_z(t) = \mathbf{M}_0 \left(1 - e^{-\frac{t}{T_1}}\right), \quad (11)$$

where T_1 represents the longitudinal relaxation constant, defined as the time needed for the recovery of longitudinal magnetization to 63% of its initial value.

Secondly, due to microscopic field inhomogeneities the precession frequencies of individual spins are slightly different. Although immediately after RF-pulse application all spins precess with the same phase, due to the variation in their Larmor frequencies, they gradually desynchronize. This process, called transversal or spin-spin relaxation, resulting in the transversal magnetization decay back to its initial, zero value, is caused by two distinct factors. First of them are molecular interactions between individual spins (spin-spin interactions). The relaxation caused by this intrinsic factor is irreversible and described by the time constant T_2 - defined as the time during which the transversal magnetization decays to 37% of its maximal value. The inhomogeneity of the static magnetic field in the imaged object represents the second factor. This relaxation is described by T_{inhom} constant and makes the \mathbf{M}_{xy} to decay much faster than in a case of simple T_2 relaxation, however, it can be reversed by using specialized pulse sequences. The time constant T_2^* includes both of these effects

$$\frac{1}{T_2^*} = \frac{1}{T_2} + \frac{1}{T_{inhom}}, \quad (12)$$

and allows to describe total transversal magnetization decay as

$$\mathbf{M}_{xy}(t) = \mathbf{M}_0 e^{-\frac{t}{T_2^*}}. \quad (13)$$

The evolution of the magnetization vector in the presence of the dynamic magnetic field \mathbf{B} (in a form of RF-pulse) is described by the Bloch equation [18]

$$\frac{d\mathbf{M}}{dt} = \gamma\mathbf{M}\times\mathbf{B} + \frac{1}{T_1}(\mathbf{M}_0 - \mathbf{M}_z) - \frac{1}{T_2}(\mathbf{M}_x + \mathbf{M}_y), \quad (14)$$

where individual terms represent the processes of excitation and subsequent relaxation of the system.

As the Bloch equation depicts, for a single excitation the strongest signal is measured if a 90° flip angle is used. When multiple RF-pulses are applied subsequently, with a periodic time delay known as repetition time (TR), only partial longitudinal relaxation occurs. Since only the already relaxed \mathbf{M}_z can be re-excited again and therefore used for signal creation, this leads to a signal loss in the subsequent excitations, whose strength depends on the TR. However, this effect can be minimized by reducing flip angle. The optimum signal-to-noise ratio (SNR) for a given combination of T_1 constant and the TR is achieved, by using Ernst flip angle [19]

$$\theta_E = \arccos\left(e^{-\frac{TR}{T_1}}\right). \quad (15)$$

2.1.5 Image creation

The easiest method of acquiring MR signal of the object is to only apply 90° RF-pulse to the whole object. This creates transverse magnetization in the object, rotating in the xy-plane with the Larmor frequency. If a coil is placed next to this sample, the oscillating magnetic field triggers the flow of electric current in the coil, which constitutes the MR signal. This signal is called Free Induction Decay (FID), as it exponentially decays in time due to the relaxation mechanisms. Although the MR signal is very weak, the knowledge of its exact frequency makes the detection possible.

In this simple setup, the whole sample provides the FID signal of the same frequency, therefore only the sample's average proton density and relaxation times can be assessed. To obtain maps of their spatial distributions (MR images), the signal has to be spatially localized. This can be achieved by subsequent application of gradient fields along all space directions, thus modifying precession frequencies of spins based on their location.

Usually, 3D MR image is created by stacking 2D images on the top of each other. In this case, the slice selection is achieved by superimposing gradient field in the z-direction (\mathbf{G}_z) over the \mathbf{B}_0 . The Larmor frequency of spins then depends on their position along z-axis (z) given as

$$\omega = -\gamma(B_0 + G_z z). \quad (16)$$

This allows exciting spins of certain z-positions only (localized slice) by applying an RF-pulse of required frequency range. Therefore, the slice thickness is given by the frequency range of RF-pulse, known as transmission bandwidth (tBW).

After certain slice is excited, the localization of signal within the xy-plane must be performed, by successive application of two additional gradient fields G_x and G_y . Since they are applied one after another, the strength (not direction) of magnetic field along x- and y-axis is modified with certain time lag. The introduction of the first gradient field, lets say G_y , causes the spins of different y-positions to precess with different frequencies. When the second gradient field is applied, the phase of spins already differ. The phase-encoding (PE) along y-axis is thus achieved. The second gradient field (G_x) is introduced during data acquisition, resulting in a modification of the measured signal frequency based on the x-position of a signal source. The so-called frequency-encoding (FE) is thus achieved. Since the frequency along a line in FE direction is then varying, to receive the signal of the whole line, the reception of certain frequency range (Δf) is required, usually expressed in terms of Δf per pixel in the FE direction, referred as the receiver bandwidth (rBW) per pixel. The choice of rBW has a huge impact on image quality, since it is inversely proportional to the minimal TE, sampling rate and SNR and also impacts the levels of susceptibility and chemical shift artifacts present. In 3D sequences, the localization along z-direction is instead of a slice-selection performed by a second PE, is shown in Section 2.4.2.3. [20]

When a spatial localization is performed, the total signal measured at certain time $S(t)$ is given as the sum of individual signals (i.e. transversal magnetizations) of all excited spins each oscillating at a different, position dependent frequency. The MR scanner directly demodulates the signal frequency as if seen from rotating reference frame, making the observed signal frequency dependent only on the source position in the FE direction. Although transversal relaxation inevitably occurs and the signal intensity decays in time as determined by T_2 constant, we will now neglect this effect as it does not influence the signal frequency. After slice selection, the signals along all z-positions of excited slice are integrated

$$M(x, y) = \int_{z_0 - \frac{\Delta z}{2}}^{z_0 + \frac{\Delta z}{2}} M_{xy0}(x, y, z) dz, \quad (17)$$

where z_0 is the z-coordinate of slice center, and Δz is the slice thickness. The measured MR signal is thus given by

$$S(t) = \int M_{xy}(\mathbf{r}) \exp\left(-i\gamma \int_0^t (\mathbf{G}(\tau)\mathbf{r}) d\tau\right) d\mathbf{r}, \quad (18)$$

which shows that it is inherently complex with the phases of individual voxels depending on the gradient strength at their locations. This can be simplified by

using so-called k-space notation in which the signal does not depend directly on time, but rather on the k-space position

$$S(\mathbf{k}(t)) = \int M_{xy}(\mathbf{r}) e^{-i2\pi\mathbf{k}(t)\mathbf{r}} d\mathbf{r}, \quad (19)$$

where \mathbf{k} represents the accumulated phase changes and is defined as

$$\mathbf{k}(t) = \frac{\gamma}{2\pi} \int_0^t \mathbf{G}(\tau) d\tau. \quad (20)$$

This notation is very convenient, since the image can be created by a simple inverse Fourier transformation of the signal measured in the k-space. As the k-space trajectory is determined by the time integral of gradient waveforms, their manipulation allows controlling the sampling path. Most often, the whole k-space is sampled on a regular 2D grid by so-called Cartesian sampling (as in the case of gradient-echo sequence, see Section 2.1.6), although any arbitrary trajectory can be used. Furthermore, special techniques using k-space undersampling have been developed (see Section 2.4.2.1), allowing speeding up the acquisition.

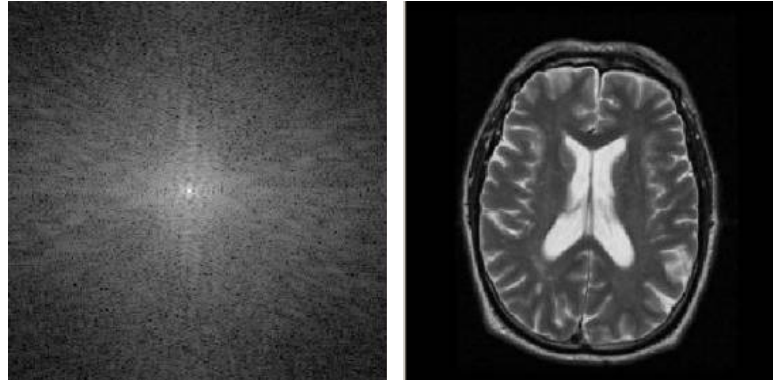


Figure 1: The image on the left depicts the acquired slice data in the k-space representation. On the right, the magnitude of the resulting image obtained by Fourier transformation is shown. (Reproduced from [21])

2.1.6 Gradient-echo sequence

Gradient-echo (GRE) is the basic MRI sequences, which uses successive application of two gradient fields of the opposite direction to create an echo. The first field causes a defocussing of spins, which are then refocused by the second gradient. Since the precession direction is still the same, the phase offsets caused by inhomogeneity of the static magnetic field in the sample are not reverted and the measured signal reflects the magnetic susceptibility of the sample. GRE sequence can be therefore used to create T_2^* -weighted image, what in the combination with the possibility of high-resolution acquisition make this sequence particularly suited for QSM imaging. Furthermore, as we will discuss later, an acquisition scheme called Echo-Planar Imaging (EPI) [2] can be used for fMRI, where susceptibility changes resulting from variations in blood oxygenation level are being observed. EPI allows for fast sampling of

hemodynamic response. The need to sample the whole of k-space with one echo train typically requires to reduce resolution and increase the sampling rate, both of which lead EPI to be sensitive to susceptibility artifacts.

The general 2D GRE sequence uses a Cartesian sampling of the k-space, filling a single line after each excitation (during one TR). After a slice selection, phase-encoding gradient selecting a certain line of k-space is introduced. Simultaneously, the negative readout gradient, i.e. frequency-encoding is applied which dephases spins along its direction. In k-space, this represents moving to the beginning of the chosen line. After some time, the readout gradient of the same intensity but opposite direction is turned on. This field refocuses spins at the time TE, known as echo time. In a next TR different PE gradient is applied, thus moving to another line of k-space.

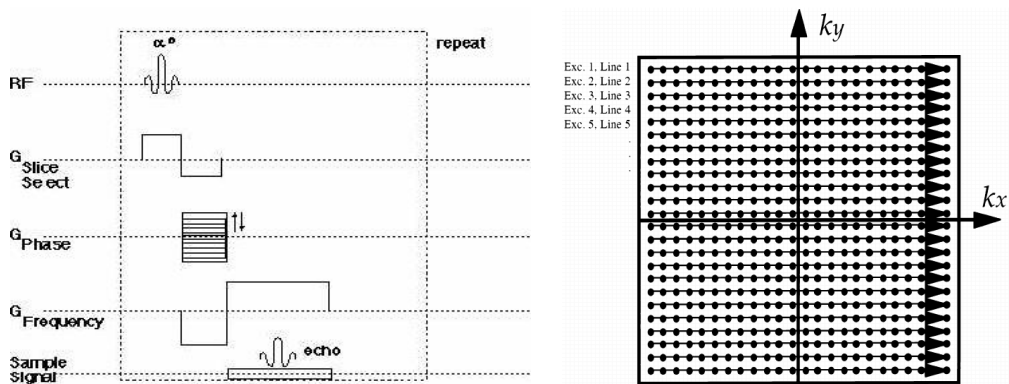


Figure 2: The pulse timing of a generic 2D gradient-echo sequence (of the left) and its corresponding k-space trajectory (on the right). During the excitation by RF-pulse, the slice selective gradient is applied. Subsequently, certain line of k-space is chosen by the phase encoding gradient and a negative readout gradient is applied to move to its beginning. The movement along the line is achieved by application of readout gradient and the signal echo is measured. (Reproduced from [22][23])

The multi-echo images can be created by repeated reversion of the readout gradient during one TR. However, as the TE increases, the relaxation of spins becomes more pronounced and the smaller signal can be measured and the associated phase images become more wrapped (see Section 2.2), since the time-dependent phase differences caused by susceptibility variation have more time to evolve. The choice of TE therefore heavily influences the sensitivity of GRE to magnetic field perturbations as well as the SNR of its phase data. To achieve the optimum phase contrast, the TE equal to the tissue's effective transverse relaxation time should be used. However, as the biological samples are usually created by many different tissue types with various $T_{2\text{ eff}}^*$, the acquisition of multiple echoes at different TEs, can be beneficial [24].

2.1.7 Ultra-high field MRI

As we have already shown (see Section 2.1.2) the stronger the static magnetic field B_0 is, the higher is the population difference as defined by Boltzmann statistics (Eq. [9]) and therefore, as given by Curie's law (Eq. [10]), the measured magnetization (MR signal) is stronger as well. The ultra-high field (UHF) MR scanners thus provide advantages of increased SNR, which can be translated into higher spatial resolution and image contrast.

Functional MRI as well as QSM benefit from the use of UHF. In fMRI, time-series SNR (tSNR) and BOLD sensitivity increase with field strength [25] [26], which allows for increase reliability of the activation results, or for the reduction of required measurement time. Moreover, at higher field strengths even small differences in the tissue's magnetic susceptibility create detectable field variations. The phase images acquired by T_2^* -weighted sequences thus show increased tissue contrast [27] and decreased noise [28].

Despite these benefits, the higher field brings also new challenges. As the susceptibility-related distortions scale with field strength, the importance of their correction increases as well. For example, the physiological noise and motion artifacts scale with image intensity, and therefore with field strength. Further, the phase of the signal across the image plane more often exceed 2π , resulting in a more higher number of "phase wraps" in the image. The phase unwrapping (see Section 2.2.1), required for visualization of the underlying anatomy, hence becomes more difficult.

The main drawback of the use of UHF scanners for phase imaging is the absence of a homogeneous volume reference coil (body coil). This makes the combination of phase data acquired by phased array receive coils challenging, as the channel dependent part of the phase offset cannot be determined from the measurement by volume reference and subsequently removed as done at lower field strengths. As we will show later (Section 2.2.4), several methods for the phase combination have been proposed.

2.2 MRI phase signal

The MR signal is inherently complex, i.e. having both magnitude and phase, however due to the difficulties of phase signal interpretation, primarily only the magnitude signal is used for imaging, leading to the loss of information encoded just in the phase.

In the recent years the huge increase in the use of methods based on the phase signal could be observed, mainly due to the increased usage of UHF scanners with strong susceptibility effects and introduction of multi-channel coils

providing high SNR [29]. Phase images allows for more sensitive depiction of neuronal demyelization and iron accumulations in the brain [30]. In phase-contrast imaging, it is used to determine the motion of spins, i.e. fluid flow velocity. Furthermore, the information about field inhomogeneity derived from phase signal can be used for distortion correction [31] [32]. The most important methods utilizing phase signal are: susceptibility weighted imaging [33] where phase information is used for contrast enhancement; susceptibility tensor imaging [34] where the orientation dependent susceptibility is characterized by an apparent susceptibility tensor and the quantitative susceptibility mapping [35] on which, we will focus in this thesis.

To create reliable phase images that allow for all these benefits is however not trivial. As the phase signal can be only in the range of $[-\pi, \pi)$, the signals of imaged object and of the background are of the same level, making the differentiation of object boundaries much more difficult. Further, as the phase develops in time, when the echo time increases the phase evolves and eventually the phase differences over the image, caused by local field variations, get higher than 2π radians. However, as the phase is a subject of a modulo of 2π , the image gets so-called wrapped, therefore containing strikes of high-intensity and low-intensity signal next to each. This confounds the visualization of underlying anatomy and raises the need for image unwrapping. Moreover, when the signal is measured by a multi-channel coil, created by an array of RF coils, the combination of signals from all channels need to be performed. However the phase measured by certain coil depends, besides the phase of interest caused by objects susceptibility (common for all channels) also on the coil sensitivity, thus making the phase signals combination very difficult. [36] [37]

In this chapter we will explain the processing steps required to achieve reliable phase images.

2.2.1 Unwrapping

The phase of measured MR signal (φ_w) at echo time TE is defined as

$$\varphi_w(\mathbf{r}) = (\gamma\Delta B(\mathbf{r})TE + \varphi_0) \bmod 2\pi, \quad (21)$$

where the first term depicts the phase component that evolves in time and the φ_0 represents all other contributions to the phase present at TE = 0. The phase signal is therefore a subject of wrapping, hampering the direct determination of the true phase (φ_{unw}), unless a very short echo time is used [38]. As the MR phase reflects the susceptibility distribution of the measured object, the exact rotation of spins in one voxel with respect to the other must be known, otherwise the over-, resp. underestimation of susceptibility would occur. Since the relation between true and measured phase is given as

$$\varphi_{unw}(\mathbf{r}) = \varphi_w(\mathbf{r}) + 2\pi n(\mathbf{r}), \quad (22)$$

the φ_{unw} can be resolved from φ_w in a process called unwrapping, by removing discontinuities in the phase image. In two large groups of unwrapping algorithms, temporal or spatial techniques, this is achieved by adding the multiples (n) of 2π radians to wrapped regions. However, the correct value of n must be determined for each voxel. As shown later in this Section, in Laplacian algorithm, which does not belong to neither of these groups, the unwrapping is achieved by solving partial differential equations and calculating derivatives using fast Fourier transforms.

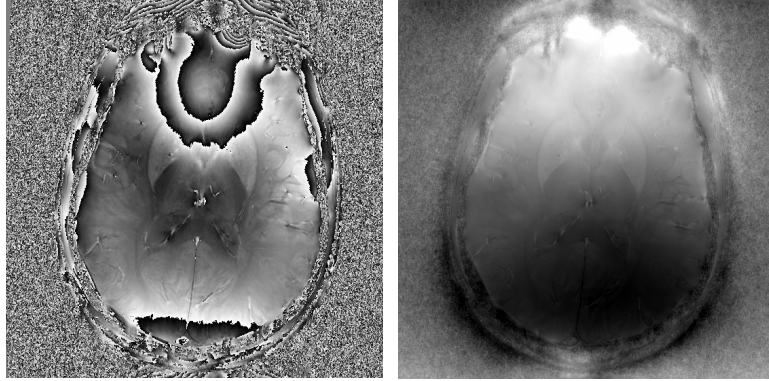


Figure 3: The wrapped phase image (on the left) and its corresponding unwrapped image (on the right) by Laplacian approach.

Temporal algorithms consider, for each voxel separately, the temporal evolution of the phase. Therefore, they can be only applied to multi-echo data and therefore cannot be used for single-echo EPI measurements.

Spatial algorithms, unlike temporal, can be also used to unwrap single-echo data since they are based on the spatial relation of phase values between neighboring voxels. The main idea behind is that since the phase gradients are usually very shallow, the phase changes slowly from voxel to voxel, unless a wrap occurs. Many different spatial algorithms have been proposed and can be further divided into two groups: path-following and Laplacian unwrapping methods.

In path-following methods a wrap is determined as the border of two neighboring voxel along the path, between which the phase changes by more than π . To retrieve the true phase, the value of $+\pi$ or $-\pi$ (for positive or negative phase jump respectively) is added to all further voxels along the path. Although these methods work well for high SNR gradient-echo phase images, which are only slowly varying in space, however they often fail when applied to more noisy data with steep spatial phase gradients or disconnected image regions.

In contrast, Laplacian unwrapping [39] [40] has been shown to be capable of unwrapping even noisy phase maps. Thanks to that and its computational

simplicity, it is often the method of choice in QSM processing. In a first step, Laplacian (Δ) of the unwrapped phase is calculated from the wrapped phase as

$$\Delta\varphi_{unw} = \text{Im}(\Delta e^{i\varphi_w} \cdot e^{-i\varphi_w}). \quad (23)$$

Then, Laplacian unwrapping attempts to identify the unwrapped phase with the local derivatives most similar to those of the wrapped phase. Additionally to the removing of phase discontinuities, the spatially slow modification of all phase values may occur, resulting in background field suppression. However, since in QSM processing the background field correction is applied, its results stay unaffected. [24] [37] [41]

2.2.2 Phase problems (open-ended fringelines)

The unwrapping of phase images may become more challenging, if so-called open-ended fringelines are present.

Wrapped phase images may contain two different types of borderlines, called fringelines and cutlines. While cutline represents the boundary of two pixels between which a real phase rotation of more than π occurs, the fringeline represents the boundary of two pixels between which phase wrapping seems to occur as the phase jumps from $+\pi$ to $-\pi$. However, the fringeline may be also cutline and therefore the measured phase may represent the true phase at both sides simultaneously.

When no cutline is present, a fringeline is closed with no open ends. In this case, the φ_{unw} can be quite easily determined at any point, since then this fringeline must have resulted from a wrapping procedure. However, when a phase image contains cutline, a fringeline has two open ends. This makes the determination of the φ_{unw} much more complicated (by conventional approaches even impossible) as the unwrapping of pixels at the fringeline ends results in phase loops, often called phase singularities or inconsistencies. [36] As we will explain later, these open-ended fringe lines may be caused by the total signal cancelation during over-channel combination of complex data.

2.2.3 Principles of phase combination

The introduction of multi-channel coils, also called phase arrays, allowed for imaging of large FOVs with high SNR and resolution and for the replacement of time-consuming Fourier encoding with sensitivity encoding, allowing "parallel imaging" acceleration. Phase array coils are created by assembling a number of small surface RF coils, each with its own preamplifier and receiver chain, simultaneously acquiring the signal from the whole FOV, however with different, spatially varying receive sensitivities. The sensitivity profiles of individual coils of the array depend on their mutual inductance and on the RF radiation

wavelength in the tissue [29].

The complex signal (S) acquired by a coil c is after Fourier transformation given as

$$S^c(\mathbf{r}, TE) = M_{xy}^c(\mathbf{r}, TE) \exp(-i\varphi^c(\mathbf{r}, TE)), \quad (24)$$

where M_{xy}^c is the product of the transversal magnetization (maximal achievable signal) at the acquisition time TE multiplied by the sensitivity profile of coil c , and where φ^c represents the phase of the channel c . The measured phase consist of a channel-dependent time constant part, so-called phase offset (φ_0^c) and a channel-independent part, which however depends on echo time

$$\varphi^c(\mathbf{r}, TE) = \varphi_0^c(\mathbf{r}) + \gamma \Delta B_0(\mathbf{r}) TE. \quad (25)$$

While the second term that originates in ΔB_0 is common for all channels, the first term is different for each channel and depends on the phase of readout gradient, gradient delay effects, eddy currents, receiver chain length and the spatially varying coil sensitivity, which is generally not known. Because of that, the phase of each channel at certain location is influenced by a noise with different strength, resulting in an unknown phase offset maps.

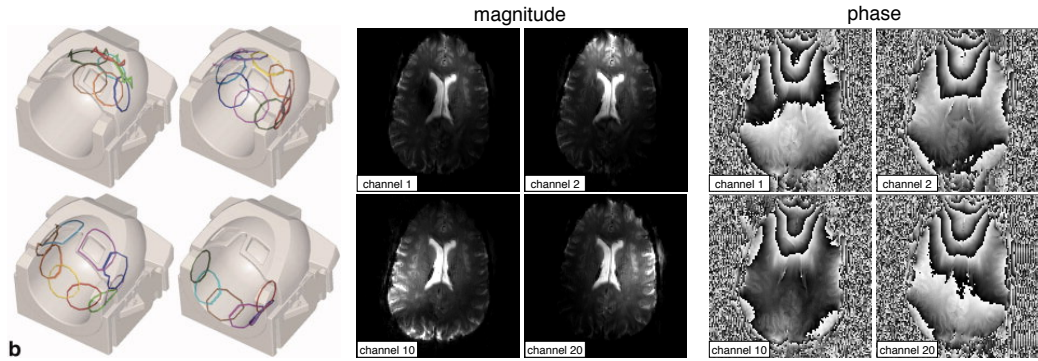


Figure 4: Left: The assembly of 32-channel head coil. (Reproduced from [42]) Right: Magnitudes and phases measured by individual coils in array (illustrated for 4 channels from a 32-channel phase-array). To show the differences in channel's sensitivity profiles, the images from spatially more distant channels are presented.

In a phase processing pipeline, the signals of individual channels must be at first brought in phase, often called as being "matched", and only then can be combined by complex summation [37]. The phase matching can be done by determining and removing of otherwise absolute $\varphi_0^c(\mathbf{r})$, hence leaving only the phase reflecting susceptibility-related B_0 changes, or of phase offsets relative to some somewhat arbitrary phase distribution, hence leaving unknown but common to all channels phase offset. However, when substantial noise is present or when the removed phase offsets are incorrect (often happens when they are only estimated, i.e. in reference-free single-echo methods), the phase-matching of channels is imperfect resulting in the signal cancelation during the complex summation. When a complete cancelation of the signal occurs, the combined

phase image contains an open-ended fringe line.

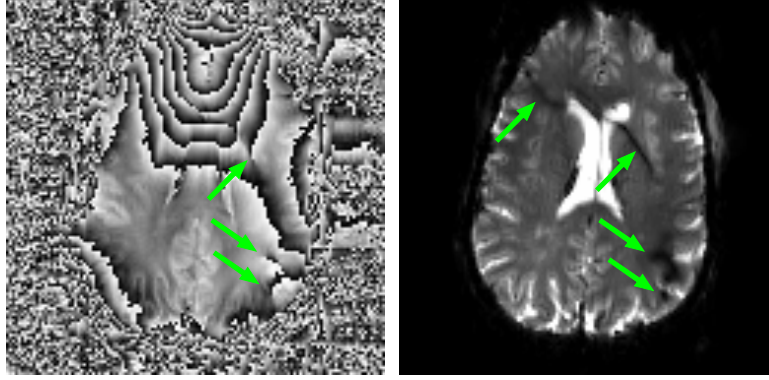


Figure 5: Phase (on the left) and magnitude (on the right) of the combined data. During the combination the complete signal cancellation occurred, resulting in a visible signal dropout in magnitude and creation of open-ended fringe lines in phase.

2.2.3.1 Combination quality assessment - Q -maps

The absence of evident phase errors is however not sufficient for evaluation of combination quality, as it does not take into account the SNR loss caused by imperfect phase matching. As there is no information about the ground truth available, it was proposed [38] to represent the quality of phase matching by a metric Q , defined as

$$Q = \frac{\left| \sum_j M_j e^{i(\varphi_{j,corrected})} \right|}{\sum_j M_j}. \quad (26)$$

When the phases of the signal vectors of all channels are matched, the length of the vector calculated by their complex sum (numerator) should be equal to the sum of the lengths of individual signal vectors (denominator). Therefore, the optimally combined data would have $Q = 1$ in all signal containing voxels and $Q = 0$ in the background, as the complex signal should cancel in the areas containing only the noise.

2.2.4 Phase combination methods

Multi-channel phase combination methods can be divided into categories based on whether they require acquisition of reference scan or not, and on whether they use single-echo or a multi-echo sequence. In this chapter, we will present some of the most commonly used or useful approaches, and then we will focus on the Virtual Reference Coil method, which was considered to be the most appropriate for the online combination of fMRI data, since it does not require reference measurement or multi-echo acquisition and has quite low computational demands.

2.2.4.1 Requiring reference-scan

A common phase-combination method, called Roemer [29] or SENSE [43], measures a reference scan by a homogeneous volume reference coil and thus determines the sensitivity profiles of each channel with respect to the sensitivity of the volume coil (individual channel sensitivities are assembled in vector \mathbf{b}). Further, the noise correlation matrix (\mathbf{R}) is calculated from a prescan without any RF excitation. The diagonal elements of \mathbf{R} represent the noise levels of individual coils and its off-diagonal elements represent the correlations between each two coils of phase-array. The complex signal of certain voxel measured simultaneously by all channels (assembled in vector \mathbf{p}) can be then combined to a single complex value (P) by

$$P = \mathbf{p}^T \mathbf{R}^{-1} \mathbf{b}. \quad (27)$$

However, because the phase offsets are not actually removed but only substituted by the phase offset of the volume coil, although the SNR of combined images is almost optimal, the phase images do not represent the true phase what may affect the subsequent QSM analysis. Moreover, due to the absence of a volume reference coil at ultra-high field scanners this method can be used only at lower field strengths. [37] [44]

Another method, called MCPC-3D-II [38] (Multi-channel phase combination using 3D phase offsets derived from a dual echo scan) calculates the phase offsets by subtracting the reference scan's phase images measured at echo times TE_1 and TE_2 . The temporal evolution over the TE_2-TE_1 is thus obtained and can be extrapolated to the $TE = 0$, when only $\varphi_0^c(\mathbf{r})$ are left. The reference images however need to be unwrapped for this calculation, however. The calculated phase offsets are then coregistered to the phase images of the main scan and subsequently subtracted. Individual channels are thus matched (free of $\varphi_0^c(\mathbf{r})$) and can be combined by weighted complex sum.

Last method we will mention in this Section, called COMPOSER [45] (Combining phased array data using offsets from a short echo-time reference), measures the reference scan with very short echo time ($\sim 1-2$ ms), thus allowing to approximate φ_0^c by $\varphi^c(TE)$, since the TE dependent part of phase gets negligibly small. Following steps are then common to MCPC-3D-II.

The possible usage of these methods is quite restricted, as the reference scans required may not be always possible to measure. Moreover, as the reference scan is acquired prior to the main scan and subsequently coregistered, all these methods are very vulnerable to motion.

2.2.4.2 Reference-free multi-echo methods

The basic multi-echo method eliminates phase-offsets of channels by calculating

Hermitian Inner Product (HiP) between the two complex images measured at echo times TE_1 and TE_2 . This can be expressed as

$$\varphi(\mathbf{r}, TE_1, TE_2) = \angle \left(\sum_c |m^c(\mathbf{r}, TE_1)| |m^c(\mathbf{r}, TE_2)| e^{-i(\varphi^c(\mathbf{r}, TE_1) - \varphi^c(\mathbf{r}, TE_2))} \right), \quad (28)$$

where m^c and φ^c represent the magnitude and the phase of the complex signal measured by a coil c . Since the phase-offsets do not depend on TE, the phase subtraction leads to their cancelation. So for each channel, a single image with phase given only by the phase evolution during the time $TE_2 - TE_1$ is created, and therefore the subsequent over-channel combination can be carried out. Although this method is very simple and does not require unwrapping, the SNR of the combined image is quite low.

In another method, called MCPC-3D-I the phase offset of each coil is calculated from its unwrapped phase images φ_{unw}^c measured at TE_1 and TE_2 using the equation

$$\varphi_0^c(\mathbf{r}) = \frac{\varphi_{unw}^c(\mathbf{r}, TE_1)TE_2 - \varphi_{unw}^c(\mathbf{r}, TE_2)TE_1}{TE_2 - TE_1}. \quad (29)$$

These phase offsets are first smoothed, to get rid of noise and other undesired effects of high spatial frequency (e.g. partial volume effects, susceptibility anisotropy) and then removed from the measured phase images prior to the combination. Because the single-channel phase images often contain open-ended fringe lines, the correct unwrapping may not be achievable, and the combination may suffer. Further, the unwrapping of all uncombined images makes this method very computationally demanding.

The last multi-echo method mentioned here is the simplification of MCPC-3D-I, called ASPIRE (A Simple Phase Image Reconstruction for multi-echo acquisitions) [46], which restricts the choice of echo-times by the condition $mTE_2 = (m + 1)TE_1$. The main idea behind is that beside the noise, the single-channel phase differences calculated by MCPC-3D-I are the same as the combined phase difference calculated by HiP, which can be written as

$$\begin{aligned} \Delta\varphi(\mathbf{r}, TE_1, TE_2) &= \varphi_{unw}^c(\mathbf{r}, TE_2) - \varphi_{unw}^c(\mathbf{r}, TE_1) \\ &= \varphi_w^c(\mathbf{r}, TE_2) - \varphi_w^c(\mathbf{r}, TE_1) \end{aligned} \quad (30)$$

This allows for rewriting of the Eq. [29] to

$$\varphi_0^c(\mathbf{r}) = \varphi_w^c(\mathbf{r}, TE_1) - \frac{TE_1}{TE_2 - TE_1} \Delta\varphi(\mathbf{r}, TE_1, TE_2). \quad (31)$$

Then, if the TE-dependent factor by which the $\Delta\varphi$ is scaled is integer, as is required by ASPIRE, the phase offsets can be calculated directly by the subtraction of HiP from the original, wrapped phase of the first echo. Their smoothing prior to the removal is however still necessary.

Even though these methods can provide reliable phase images, their use is

restricted only to the multi-echo data and depending on the used method, further echo-spacing constrains may be applied.

2.2.4.3 Reference-free single-echo methods

The adaptive combine method (AC) [47] uses localized estimates of coil sensitivities for the combination of complex images. Directly from the measured individual channel images, containing both noise and relevant signal, the correlation matrices \mathbf{R} for all voxels (as in Roemer method) are determined by averaging complex image cross-products over local image regions and then they aligned to the vector. Then, an optimal filter vector that maximizes the expected SNR for the calculated vector of \mathbf{R} s is determined by optimization process and applied before the combination. AC therefore works well for magnitude images yielding almost optimal SNR even without a-priori knowledge of the coil sensitivity maps, but often leads to errors and inconsistencies in combined phase.

Another approach, called scalar phase matching (SPM) or Hammond method [48], approximates the spatially slowly varying phase offset of each channel by a constant value. This constant offset is for each channel at first determined as the phase of the channel's voxel located in a predefined region (matching region of interest - ROI_M), in which the sum of magnitudes of all channels is highest, and then subtracted from the whole single-channel image prior to their combination. The estimated values of phase offsets have however significant influence on the following combination and therefore the ROI_M has to be chosen carefully. It should be localized close to the object's center, should not contain wraps and all channels should have sufficient signal in it. Different approaches to the choice of ROI_M center were suggested, e.g. central voxel of the image [48] or voxel with the maximal product of single-channel magnitudes [49], however the definition of single, best approach that would provide reliable value in all cases is very difficult, as it depends on the sample's anatomy. Moreover, although the channel-dependent phase offsets are generally only very slowly varying in space, they are not constant as approximated by SPM. Their variation increases with decreasing RF wavelength and with increasing distance from ROI_M , therefore resulting in an increased error caused by this approximation. When this error gets too big, as in the case of higher field strengths or larger objects, the errors in the combined phase occurs. [37]

The SPM can, however, be used to create a virtual reference coil (VRC) image to which the phases of all channels are referenced before combination. The virtual reference coil therefore plays the role of the volume coil in Roemer method. This method is known as VRC [14] and will be described in depth in the following Section.

The main benefit of reference-free single-echo approaches is that they are very general and can be used in any case, since they do not pose any special requirement on the sequence neither require additional reference scan measurement. However, they are inherently unable to determine the real phase offsets and therefore, similarly to Roemer method, the $\varphi_0^c(\mathbf{r})$ are not removed completely but only substituted by the unknown phase offset common to all channels. The combined phase therefore does not reflect only ΔB_0 , but introduces additional phase sources, which in reality do not exist. Following analysis (e.g. QSM) may be therefore influenced and the results may not reflect the reality [50].

2.2.5 Virtual Reference Coil method

Virtual reference coil (VRC) method [14] is a very general, reference-free phase combination method that does not pose any special requirements on the measurement and that can reach very high combination quality. Furthermore, because it does not require unwrapping, its computational demands are quite low and therefore it can be used to perform online combination directly on MR scanner reconstruction unit.

Common to Roemer method, VRC references the phase of each channel to a single coil that is sensitive over the whole imaged volume. In VRC however, this coil is only virtual. Since it is generated directly from the measured, separate-channel data, VRC method can be used even if the volume coil is not available. The processing steps of VRC approach are illustrated in Figure 6 and referenced in the following description.

The phase measured by a coil c (φ^c) is given as the sum of the true tissue phase of interest ($\theta(\mathbf{r}) = \gamma \Delta B_0(\mathbf{r})TE$) with the undesired time-constant phase offset of the coil (φ_0^c) and time-varying, random phase caused by thermal noise (n^c):

$$\varphi^c(\mathbf{r}) = \varphi_0^c(\mathbf{r}) + \theta(\mathbf{r}) + n^c(\mathbf{r}). \quad (32)$$

In the original VRC approach, the virtual reference coil (v) is created by scalar phase matching. As explained in the previous chapter, at first the ROI_M is defined as a region located close to the image center and with sufficient sensitivity of all channels. Then, a voxel (often referred as VRC center) from the ROI_M , in which there is a maximum overlap of the signals from all coils is found (localized at position x_0) and its phase, given by

$$\varphi_{x_0}^c = \varphi_0^c(x_0) + \theta(x_0) + n^c(x_0) \quad (33)$$

approximating the phase offset of the channel is then subtracted from the measured phase (step 1). This sets the phase of each channel at the VRC center, i.e. centers the image, to zero, and leaves the phase (φ_{cent}^c) given as

$$\begin{aligned} \varphi_{cent}^c(\mathbf{r}) &= \varphi^c(\mathbf{r}) - \varphi_{x_0}^c \\ &= \varphi_0^c(\mathbf{r}) - \varphi_0^c(x_0) + \theta(\mathbf{r}) - \theta(x_0) + n^c(\mathbf{r}) \end{aligned} \quad (34)$$

Then, the virtual reference coil (v) is created by the complex combination of centered images (step 2). Away from the ROI_M the phase-matching quality is quite low resulting in a low SNR of the VRC, however, all the phase contrast common to all channels is contained and the phase (φ^v) is defined by

$$\varphi^v(\mathbf{r}) = \varphi_0^v(\mathbf{r}) + \theta(\mathbf{r}) + n^v(\mathbf{r}). \quad (35)$$

The creation of the virtual reference coil (v) can be thus expressed as a weighted complex combination of the individual-channel measurements

$$v(\mathbf{r}) = \sum_c w^c(\mathbf{r}) \varphi^c(\mathbf{r}), \quad (36)$$

with the weights chosen based on SNR of measured single-channel complex images. When the optimal weights are used, the VRC with higher SNR than any of the channels has, can be created. In the work by Parker [14], the magnitude weighting was suggested, however due to error in the description it was omitted and therefore not used. In original VRC approach, only the optimal weights for phase given by $\varphi_{x_0}^c$ are used, resulting in

$$v(\mathbf{r}) = \sum_c |w^c(\mathbf{r})| e^{i\varphi_{x_0}^c(\mathbf{r})} e^{i(\varphi_0^c(\mathbf{r}) + \theta(\mathbf{r}) + n^c(\mathbf{r}))}. \quad (37)$$

When the VRC is created, all single-channel measurements can be referenced to it (step 3). This eliminates the true phase, leaving only the differences between the channels' phase offsets and thermal noise components

$$\varphi^{vc}(\mathbf{r}) = \varphi_0^c(\mathbf{r}) - \varphi_0^v(\mathbf{r}) + n^c(\mathbf{r}) - n^v(\mathbf{r}). \quad (38)$$

Further, because the phase offsets are generally only slowly spatially varying, the high frequency noise can be suppressed by smoothing i.e. spatial low-pass filtering (denoted by $\langle \cdot \rangle$) (step 4), therefore leaving only the difference of phase offsets.

$$\langle \varphi^{vc}(\mathbf{r}) \rangle = \varphi_0^c(\mathbf{r}) - \varphi_0^v(\mathbf{r}) \quad (39)$$

The smoothing has to be applied in the complex space, i.e. smoothing the real and imaginary parts separately, as the smoothing of wrapped phase would result in the undesired smearing of the wraps. The relative phase offset of each channel (w.r.t to the VRC) is thus created and can be subsequently removed (step 5), introducing the channel independent VRC's phase

$$\begin{aligned} \varphi^c(\mathbf{r}) &= \varphi_0^c(\mathbf{r}) + \theta(\mathbf{r}) + n^c(\mathbf{r}) - \langle \varphi^{vc}(\mathbf{r}) \rangle \\ &= \varphi_0^v(\mathbf{r}) + \theta(\mathbf{r}) + n^c(\mathbf{r}). \end{aligned} \quad (40)$$

Since the measured phase is except of the very small noise term independent of the channel, the phase-matching is achieved and the final combination can be carried out (step 6). As Eq. [40] depicts, although excellent phase-matching quality can be reached, the combined phase differs from the true phase by the (generally slowly varying) phase of VRC.

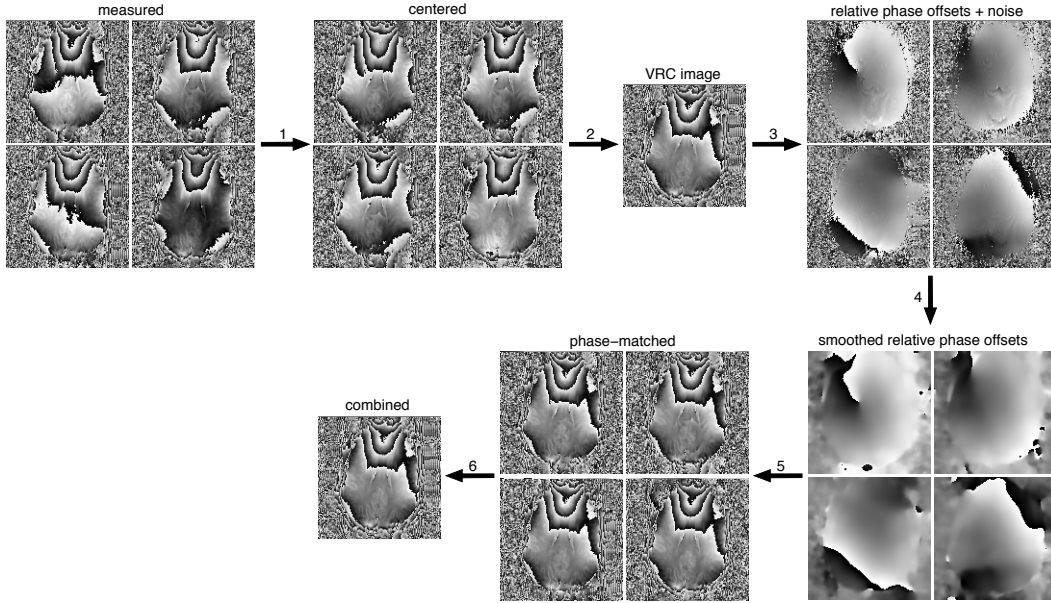


Figure 6: The main steps in VRC combination approach (illustrated for 4 channels from a 32-channel phase-array). At first, from each of the phases measured by individual coils in array the value of its center is removed. Then, the VRC image is created by magnitude weighted combination of these centered phases. By referencing of measured phases to this VRC image, the relative phase offsets however containing also the thermal noise component are determined. By removing of smoothed (i.e. noise suppressed) relative phase offsets from the measured phases the phase-matching is achieved and by magnitude weighted combination of matched and subsequently smoothed (for noise suppression) phases, the final image is created.

The quality of the phase-matching is critically dependent on the quality of created VRC, therefore the method fails when the VRC image contains open-ended fringe lines. As we have already mentioned, SPM often breaks down when used for large objects at higher field strengths, making the VRC to break down as well. Nevertheless, in all cases when SPM is capable of creating a reliable virtual coil image, VRC method can be applied as well, providing better combination quality. This is due to the fact, that although VRC image created by SPM has low SNR away from the ROI_M , all phase contrast common to all channels is contained. The difference between the phase of each channel and the VRC is thus small and the SNR of combined image is higher than in SPM. [37]

To address the problems associated with using SPM for creating virtual reference coil, different methods have been proposed and might provide reliable results even in the case when SPM breaks down. Simple approach, to which we will refer as magnitude-weighted SPM (mwSPM), multiplies the measured complex signal of each channel by its magnitude, approximating the coil sensitivity, prior to the combination. The magnitude weighting can be applied in both combination steps, e.g. when virtual reference coil and when final combined image are being created, resulting in the noise suppression and therefore SNR increase. Although this approach was suggested by Parker et al [14], it was not used in their study, due to error in the equation derivation. As we will show in this thesis, this approach yields very high combination quality over the whole

brain. Another method, called Virtual body coil (VBC) method [51], uses singular value decomposition to create VBC, which is then similarly used for phase referencing, however the robustness of this method have not been yet fully tested.

2.3 Quantitative Susceptibility Mapping

Magnetic susceptibility is the macroscopic physical property that describes the change in magnetization of the sample when placed in an external magnetic field. Quantitative susceptibility mapping (QSM) allows extracting the spatial distribution of bulk magnetic susceptibility within the objects, using MRI phase data. In the brain tissue, the magnetic susceptibility is mainly determined by absolute content and distribution of water, myelin, iron and calcium. While myelin and calcium are more diamagnetic than water, therefore have lower susceptibility, the susceptibility of blood iron is relatively higher. In QSM, the susceptibility values are not determined in an absolute way but rather given relative to a reference region, whose choice may thus significantly influence the results. Further the QSM values have been shown to depend on the echo time in a non-linear fashion with their relation influenced by the tissue microstructure [52] and the white matter's susceptibility was also shown to be orientation dependent [53]. Nevertheless the QSM provides a novel contrast, with a high sensitivity to iron, calcium and myelin.

In recent years, the field of QSM has greatly developed thanks to the advent of ultra-high field MRI resulting in an increased sensitivity of T_2^* -weighted sequences to magnetic susceptibility differences. QSM analysis is carried out in three main steps: estimating magnetic field distribution from the combined MRI phase data, applying a so-called background field correction in which field contributions not caused by susceptibility sources located in the region of interest are eliminated, and converting the field pattern to the susceptibility map by solving the inverse problem of the deconvolution of internal magnetic field distribution with the unit dipole response (see Section 2.3.3). In general, many different algorithms for each step of QSM processing exist and are reviewed in [41]. In this thesis, the algorithm based on total generalized variation (TGV) [5], integrating all QSM's steps into one will be described in more details (Section 2.3.4).

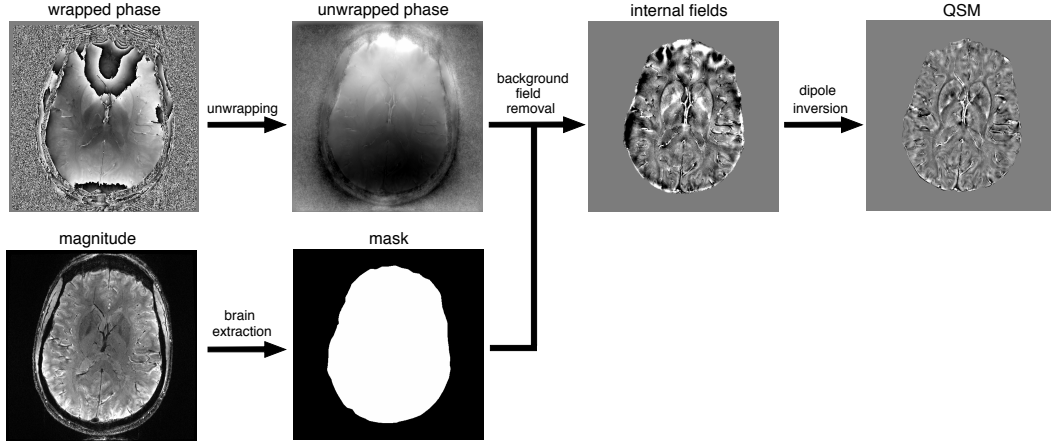


Figure 7: The main steps in QSM analysis. The field map is estimated from the combined wrapped phase by phase-unwrapping and subsequent dividing by the factor γTE (Eq. [41]). Then, out of magnitude image a brain mask is created and applied during the background field removal. Finally, the QSM is obtained by dipole inversion, i.e. by solving of the ill-posed problem of the deconvolution of the magnetic field distribution with the unit dipole response.

2.3.1 Estimation of the magnetic field distribution

In order to estimate the magnetic field distribution, the measured combined phase data have to be at first unwrapped using one of the many algorithms available (see Section 2.2.1). Subsequently, the magnetic field distribution (ΔB_0) is estimated as

$$\Delta B_0(\mathbf{r}) = \frac{\varphi_{unw}(\mathbf{r}, TE)}{\gamma TE}. \quad (41)$$

However, when the phase offset is not completely removed during combination process and the unknown phase offset ($\varphi_0^v(\mathbf{r})$) is left, as in the case of reference-free single-echo approaches (e.g. VRC method, Eq. [40]), the ΔB_0 is given as

$$\Delta B_0(\mathbf{r}) = \frac{\varphi_{unw}(\mathbf{r}, TE)}{\gamma TE} + \frac{\varphi_0^v(\mathbf{r})}{\gamma TE}, \quad (42)$$

thus contains additional, undesired field offset. The error caused by this phase offset thus propagates to further QSM steps but can be suppressed by some of the known background field removal approaches. [41]

2.3.2 Background field removal

The MRI measurement is restricted to a certain region (FOV), therefore only the signal originating from this FOV is acquired. The signal's phase at each location depends on total magnetic field perturbation at that place, which is however influenced by the magnetic susceptibility distribution throughout the whole space, including sources located outside of the FOV. Moreover, the inhomogeneities of the external magnetic field of the scanner and of shimming fields also contribute to the ΔB_0 .

The estimated magnetic field distribution can be thus decomposed into field

contributions generated by the susceptibility sources within the FOV (ΔB_{int}) and by the field contributions out of interest, so-called background field (ΔB_{bg})

$$\Delta B_0(\mathbf{r}) = \Delta B_{int}(\mathbf{r}) + \Delta B_{bg}(\mathbf{r}). \quad (43)$$

Since the background field consists of the fields created by susceptibility sources located outside FOV (e.g. skull, sinuses, torso) and the scanner fields' imperfections, its magnitude is usually 10-100x larger than of ΔB_{int} . Therefore, to determine the susceptibility distribution out of estimated magnetic field distribution, one of known approaches (reviewed in [24] [41]) for efficient removing of the background field has to be applied, before the dipole inversion can be carried out.

2.3.3 Dipole inversion

When a sample is placed into the static magnetic field \mathbf{B}_0 , after a short time the thermal equilibrium is achieved. The magnetization of the sample is created and acts as the source of an additional field. This, so-called demagnetization field, depends on the strength and direction of the \mathbf{B}_0 as well as on the sample's magnetic susceptibility distribution $\chi(\mathbf{r})$, determined by its material composition, internal structure and geometry.

If a distance between the location of demagnetization field source (\mathbf{r}_i) and the observation point (\mathbf{r}) is large compared to its spatial extent, the magnetic field of each atom can be approximated by the magnetic field of a dipole (\mathbf{b}_d) given as

$$b_d(\mathbf{r}, \mathbf{m}) = \mu_0 \begin{cases} \frac{3\hat{r}(\mathbf{m} \cdot \hat{r}) - \mathbf{m}}{4\pi r}, & \mathbf{r} \neq 0 \\ \frac{2}{3}\mathbf{m}, & \mathbf{r} = 0 \end{cases} \quad (44)$$

where \hat{r} is a unit vector parallel to \mathbf{r} and \mathbf{m} is the dipole moment. The demagnetization field (\mathbf{B}_{demag}) could be thus calculated by summing the magnetic fields all atoms as

$$\mathbf{B}_{demag}(\mathbf{r}) = \sum_i \mathbf{b}_d(\mathbf{r} - \mathbf{r}_i, \mathbf{m}_i), \quad (45)$$

but, that becomes very difficult for the macroscopic samples. In this case, the summation can be simplified by using Lorentz approach, where the environment surrounding the observation point is separated into near region (V_n) and distant region (V_d) by a Lorentz surface, which is for the simplicity defined as a sphere, larger than the mutual distance of adjacent magnetic moments. Due to the temporal and spatial averaging that occurs in the spin system, the Lorentz approach allows treating the magnetic moments in the V_d as a continuum and therefore the sum in Eq. [45] can be replaced by an integral over a continuous macroscopic magnetization. However, the magnetic moments in V_n have to be

treated as individual sources whose contributions to the \mathbf{B}_{demag} depend on their positions and orientations relative to \mathbf{r} . In isotropic samples, the magnetic moments average to zero, so their susceptibility depends only on the observation point, i.e. position within the sample. However, this is not the case for anisotropic materials, such as lipid bilayers or white matter fibers, whose susceptibilities are hence dependent on their orientations with respect to \mathbf{B}_0 .

For material with $|\chi| \ll 1$ placed in a static magnetic field oriented in a z-direction, the distant field (\mathbf{B}_d) at the position $\mathbf{r} \neq 0$ can be written as

$$B_d(\mathbf{r}) = B_0(\mathbf{r}) \int_{V_d(\mathbf{r})} \chi(\mathbf{r}') b_\chi(\mathbf{r} - \mathbf{r}') d^3\mathbf{r}', \quad (46)$$

with b_χ defined as

$$b_\chi(\mathbf{r}) = \frac{3\hat{r}(\hat{z} \cdot \hat{r}) - \hat{z}}{4\pi r^3} \cdot \hat{z} = \frac{3 \cos^2 \theta - 1}{4\pi r^3}, \quad (47)$$

where \hat{z} is a unit vector parallel to z and θ depicts the angle between \mathbf{r} and \mathbf{z} . For the isotropic materials, whose demagnetization field is given only by the distant field, the total magnetic field is equal to

$$B_{total}(\mathbf{r}) = B_0(\mathbf{r}) + B_d(\mathbf{r}) = B_0(\mathbf{r}) + B_0(\mathbf{r})\{\chi(\mathbf{r}') \otimes \overline{b}_\chi(\mathbf{r})\}, \quad (48)$$

with \otimes denoting the convolution and

$$\overline{b}_\chi(\mathbf{r}) = \begin{cases} b_\chi(\mathbf{r}), & \mathbf{r} \neq 0 \\ \frac{2\mu_0}{3}, & \mathbf{r} = 0 \end{cases} \quad (49)$$

Eq. [48] is the fundamental equation of current QSM techniques, describing the effect of a spatially variant magnetic susceptibility of the sample on the total magnetic field. It shows, that the determination of the susceptibility distribution can be achieved by deconvolving the magnetic field distribution (estimated in the first step of QSM) with the unit dipole response \overline{b}_χ . Since the \overline{b}_χ does not account for the susceptibility anisotropy, its effects are in QSM nowadays neglected.

The convolution in Euclidean space can be written as a simple point-wise product in the Fourier domain. The Eq. [48] can be thus rewritten to

$$FT\left(\frac{B_{total}(\mathbf{r}) - B_0(\mathbf{r})}{B_0(\mathbf{r})}\right) = FT(\chi(\mathbf{r}')) \cdot FT(\overline{b}_\chi(\mathbf{r})), \quad (50)$$

where the term on the left is often referred as the relative difference field (B_{RDF}) and represents the measured quantity. The determination of the susceptibility distribution is then formulated as an inverse problem

$$\chi(\mathbf{r}') = FT^{-1}\left(\frac{FT(B_{RDF}(\mathbf{r}))}{FT(\overline{b}_\chi(\mathbf{r}))}\right), \quad (51)$$

where the Fourier transform of the point-dipole function is defined as

$$FT(\overline{b}_\chi(\mathbf{r})) = \overline{b}_\chi(\mathbf{k}) = \begin{cases} \frac{1}{3} - \cos^2 \psi, & \mathbf{k} \neq 0 \\ 0, & \mathbf{k} = 0 \end{cases} \quad (52)$$

with ψ representing the angle between \mathbf{B}_0 and \mathbf{k} . As this equation depicts, on a conical surface in the Fourier space defined by so-called magic angle ($\psi = 54.74^\circ$), the $\overline{b}_\chi(\mathbf{k})$ is equal to zero rendering the inverse problem undetermined. Many different algorithm for solving this ill-posed problem have been suggested [Schwesser 2015], relying either on the acquisition of multiple measurements using different relative orientations [54] of the sample to the \mathbf{B}_0 or on the regularization. In this thesis, the regularization algorithm using total generalized variation penalty was applied, as will be described in the following section.

2.3.4 Total Generalized Variation based QSM algorithm

Iterative QSM reconstruction algorithm based on the total generalized variation (TGV) [55] created by Langkammer et al. [5] combines all QSM processing steps into a single integrated step. As we will explain, the susceptibility maps are reconstructed by solving an optimization problem given as

$$\min_{\chi, \psi} \int |\psi|^2 dx + TGV_\alpha^2(\chi). \quad (53)$$

In this approach, the dipole inversion, i.e. the retrieve of susceptibility distribution, is performed by TGV-regularized deconvolution of given magnetic field distribution with a dipole kernel, which can be written as

$$\frac{1}{3} \frac{\partial^2 \chi}{\partial x^2} + \frac{1}{3} \frac{\partial^2 \chi}{\partial y^2} - \frac{2}{3} \frac{\partial^2 \chi}{\partial z^2} = \frac{\Delta \varphi_{unw}}{2\pi\gamma B_0 TE}, \quad (54)$$

where $\Delta \varphi_{unw}$ represents the Laplacian of the unwrapped phase calculated directly from the wrapped phase (Eq. [23]). To incorporate the background field removal into the regularization process for the dipole inversion, an additional variable ψ is introduced, whose Laplacian is defined as the discrepancy of the dipole inversion equation on the brain mask (Ω)

$$\Delta \psi = \frac{1}{3} \frac{\partial^2 \chi}{\partial x^2} + \frac{1}{3} \frac{\partial^2 \chi}{\partial y^2} - \frac{2}{3} \frac{\partial^2 \chi}{\partial z^2} - \frac{\Delta \varphi_{unw}}{2\pi\gamma B_0 TE} \text{ in } \Omega. \quad (55)$$

Then solving the optimization problem given by the Eq. [53] with respect to ψ results in the background field removal.

By subsequent minimization with respect to χ , dipole inversion is performed, which is regularized by the second order TGV. The TGV function itself represents a minimization problem, which is performed over all vector fields (w) of the brain mask and given as

$$TGV_\alpha^2(\chi) = \min_{w \in \Omega} \alpha_1 \int_\Omega d(\nabla \chi - w) + \alpha_0 \int_\Omega d\left(\frac{1}{2}(\nabla w + \nabla w^T)\right), \quad (56)$$

where ∇ denotes the gradient and α represents the ratio of weighting parameters α_1 and α_0 , i.e. $\alpha = \alpha_1/\alpha_0$. The second order TGV thus balances between $\nabla\chi$ and $\nabla^2\chi$, as determined by α . When the $\nabla\chi$ is locally smooth, w is approaching $\nabla\chi$ resulting in a $TGV_\alpha^2(\chi) \approx \alpha_0 \int_{loc} \nabla^2 u$. On the other hand, when the $\nabla\chi$ locally jumps, ideally $w = 0$, resulting in $TGV_\alpha^2(\chi) \approx \alpha_1 \int_{loc} \nabla u$. For MRI images, it was shown that the best results are produced when α ranges between 2 and 3 [56]. Since the susceptibility distribution in the brain can be considered as smooth, using the second order TGV, which favours smoothness, it is possible to create more natural images.

When QSM processing is carried out in separate steps as done usually, the errors between the steps propagate, e.g. errors from the background field removal negatively influence the dipole inversion. Their integration into a single optimization step, as done in this algorithm, thus results in a more robust reconstruction with respect to low SNR. This may be beneficial when QSM processing of EPI data is carried out [5].

2.4 Functional Magnetic Resonance Imaging

Functional magnetic resonance imaging (fMRI) [57] [58] is a neuroimaging technique using MRI to indirectly map neural activation associated with different types of stimulations or occurring under resting condition (resting state networks). To observe the activation pattern, different types of measurement can be used. The majority of current fMRI studies however measure blood-oxygenation-level dependent (BOLD) signal, where the changes of the ratio between the oxygenated and deoxygenated blood result in the intensity variations of T_2^* -weighted images.

Compared to other neuroimaging methods like PET or EEG, the main benefits of fMRI are the quite high temporal resolution (up to few hundreds of ms) and spatial resolution (less than 1x1x1 mm), as well as the non-invasiveness of this technique. However, as the BOLD signal has no standardized base level value, data has to be acquired during both stimulation and rest period. Because the differences between their intensities are very small, the acquisition under both conditions has to be repeated many times and the data have to be subsequently statistically analysed to differentiate between the activation triggered signal changes and noise.

2.4.1 Blood-oxygenation-level dependent contrast

BOLD contrast originates in the susceptibility difference between the oxygenated (oxyHb) and deoxygenated (deoxyHb) hemoglobin. When diamagnetic oxyHb

with negative χ gives up its oxygen, the paramagnetic deoxyHb with positive χ is created. As demonstrated by Ogawa et al. [59] [60], the presence of deoxyHb in blood produces a susceptibility difference between the vessel and surrounding tissue, resulting in a local field inhomogeneity around the vessel. The use of gradient-echo sequence allows to encode these field perturbations in a variation of precession frequencies of nearby spins, resulting in dephasing within a voxel (even at the TE) and hence in a signal decrease. These intensity losses, which extend beyond the boundary of the blood vessel (as does the field variation), are the source of BOLD contrast. As was further shown by Ogawa et al. [59] [60] the size of the susceptibility-induced local field depends both on the concentration of deoxyHb and on the orientation of the vessel relative to the main magnetic field.

The change in the MR signal intensity caused by neuronal activation is called hemodynamic response. The change in the total amount of deoxyHb in voxel over time depends not only on the oxygen extraction by neurons (CMRO₂ - cerebral metabolic rate of oxygen), but also on the changes of cerebral blood flow (CBF) and cerebral blood volume (CBV). Immediately after neural activation, the increase in oxygen consumption by neurons causes very small initial dip of the signal. Although that is usually unobservable, it triggers the inflow of oxygenated blood to the area of activation, which is higher than neuronal consumption thus resulting in overall oxyHb concentration increase and thus in a global signal increase. The signal increase is visible usually ~2s after the stimulus application and reaches its maximum after ~5s. When stimulation persists, the signal "plato" occurs, with intensity only slightly lower than the maximal. When the stimulation is stopped, the undershoot (decrease under the base-level) of the signal occurs, followed by a slow return to the initial value. [16] [61]

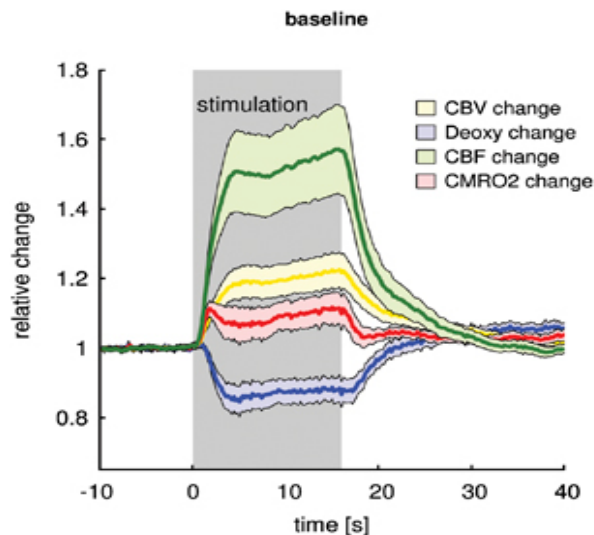


Figure 8: The time-course of individual processes that sum up to create hemodynamic (BOLD) response following the neural activation. (Reproduced from [62])

2.4.2 Echo-planar imaging sequence

To capture the brain function, it is required to acquire the images very rapidly, within the timescale of the physiological changes. For this purpose, special fast sequences have been developed, which are usually based on gradient-echo sequence and are therefore sensitive to T_2^* contrast. The most often used sequence for fMRI is echo-planar imaging (EPI) [2] which can use both gradient-echo or spin-echo technique to create a measurable signal. Because phase offsets caused by local field inhomogeneities are not (for the spin-echo not fully) reverted, the BOLD signal can be measured.

2.4.2.1 2D echo-planar imaging

In a general 2D EPI sequence, the signal from the whole k-space of a certain slice is collected after application of single RF pulse, by using an oscillating readout gradient. When readout of one k-space line is finished a short pulse of the phase-encoding gradient is applied to move to the next line in the PE direction, resulting in a long readout time in this dimension. Due to the spatial encoding with gradient fields, the local field inhomogeneities in the \mathbf{B}_0 cause signal mislocalizations and thus geometric distortions in images. Because of the EPI's long readout, the phase caused by local field inhomogeneities has time to evolve, making the EPI very prone to geometric distortions. [16] [63]

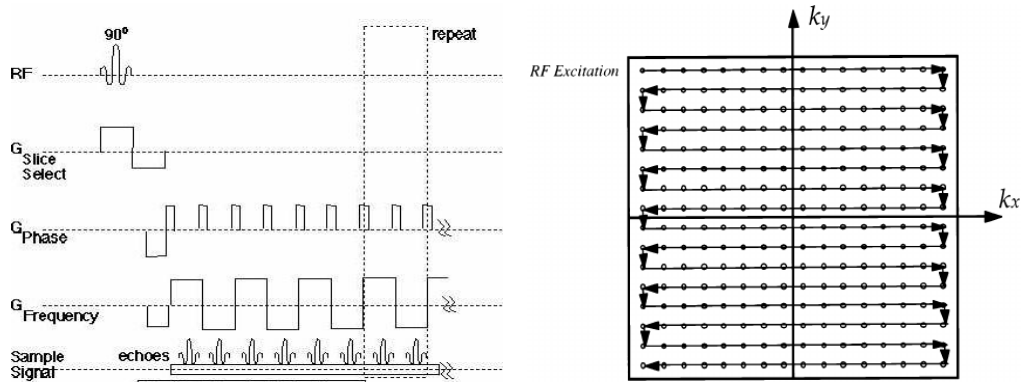


Figure 9: The pulse timing of a generic 2D gradient-recalled echo-planar imaging sequence (of the left) and its corresponding k-space trajectory (on the right). During the excitation by RF-pulse, the slice selective gradient is applied. Subsequently, the whole k-space is sampled by using oscillating frequency-encoding, i.e. readout gradient. After a certain k-space line is acquired a short pulse of the phase-encoding gradient is applied to move to the next line. (Reproduced from [22][23])

The EPI fills the k-space with a back and forth (zigzag) trajectory, meaning that the alternating lines are acquired in opposite directions. Thereby the reordering of the data has to be performed before the Fourier transformation is applied. However, because the gradient amplitudes and switching rates are in EPI quite high, large time-dependent eddy currents are induced, resulting in time-dependent frequency shifts. These shifts create a phase difference from line to

line in the raw data, resulting in a phase ambiguity after Fourier transformation and therefore signal mislocalization, creating an artifact called "ghosting". Due to the long readout period of EPI, this artifact can be very pronounced and because of the k -space zigzag trajectory, a part of the signal appears 90° out of phase, resulting in a mislocalization by one half of the image, hence creating the so-called "N/2 ghosting". As we will show in Section 2.4.3, to get rid of artifact one of the special corrections have to be applied. [43]

Since EPI is a single shot method, all of the longitudinal magnetization may be used in image formation without a penalty in overall imaging time EPI. Further, the signal may be collected for more than 75% of the imaging time, resulting in a very high efficiency. Finally, the fast repetition time of EPI leads to a reduced motion artefacts compared to images acquired by slower sequence.

In MRI, the resolution depends on the maximal achievable product of gradient amplitude and time. As the gradient power requirements of EPI are quite high, their rapid switching may cause safety issues of peripheral neural stimulation and increased noise levels. However, to increase the resolution in the PE direction simply the duration of the echo planar readout can be extended, but for the price of increased bandwidth per pixel and minimal TE. Although the geometric distortions then extend over more pixels from their source field inhomogeneity, their distance in millimeters remains constant.

To increase the resolution along the readout axis, methods reducing the amount of k -space data acquired and therefore the number of echoes (referred as echo train length) can be used. The partial Fourier (PF) method [64] [65] is based on Hermitian symmetry property of k -space. The main idea is that since the reflections about the axes in k -space are complex conjugates, it is necessary to acquire only one half of the k -space. Then, before the Fourier transformation is applied, the second half can be calculated to form a complete MR image. Acquiring only 1/2 of the data along the long readout direction therefore allows increasing the resolution along this axis. [63] [66]

A large group of methods called Parallel Imaging (PI) allow for acceleration of the image acquisition or the resolution increase. These methods are reconstruction algorithms capable of reconstructing unaliased image with the full FOV from the k -space data undersampled in PE direction. The fact that the data are acquired by an array of RF coils with individual sensitivity profiles, provides additional information for the image reconstruction. These algorithms can be separated into main groups. While GRAPPA algorithms [67] reconstruct the missing k -space data, SENSE algorithms [43] work directly on the aliased images. For SENSE, the coil sensitivity profiles must be known and are usually obtained using a prescan. The main idea behind GRAPPA is that because of the convolution of the object's and coil sensitivity profile's k -spaces, the smearing

pattern in the image k-space is created. Some information about any k-space point is thus contained in its neighbouring points as well and hence the skipped data can be calculated from the portions that were acquired. [68]

In the general 2D EPI, although both PF and PI can be applied to decrease echo time, their effectiveness for the reduction of TR is rather limited, as the acceleration can be performed only along single PE direction and therefore, the fMRI's contrast preparation period, which can even exceed the duration of the EPI echo train, has to be still applied. When a high-resolution fMRI is desired, also the number of slices required for the same volume coverage increases, resulting in a significant increase in the volume TR. This makes the achievable sampling frequency of the 2D EPI in high-resolution mode quite restricted. To address this issue, the acceleration in the z-direction has to be achieved. [66]

2.4.2.2 2D simultaneous-multi-slice echo-planar imaging

The multiband (MB) technique, also referred as simultaneous-multi-slice (SMS), was firstly introduced for EPI by Nunes et al. [69]. It uses a multiband RF pulse, which allows for selective excitation at multiple frequencies, therefore simultaneous measuring of several slices over the same pulse repetition time. A linear combination of the signals from all simultaneously excited slices is then acquired, where the signal received by each channel of phase array coil is weighted by its sensitivity profile. This signal is subsequently unaliased using PI principles, allowing for the reconstruction of the signal from individual slices.

In contrast to PI, as in SMS approach is each slice excited and sampled identically, no SNR loss caused by reduced data collection is present. However, the difficulties in unaliasing of closely spaced simultaneously acquired slices cause the SNR reduction as well. To make the unaliasing easier, the inter-slice image shifts in the PE direction increasing the distance between aliasing pixels can be introduced. In a method called CAIPIRINHA [70], these shifts are introduced by applying sign and amplitude modulated slice-selective gradient blips simultaneously with the EPI phase encoding blips.

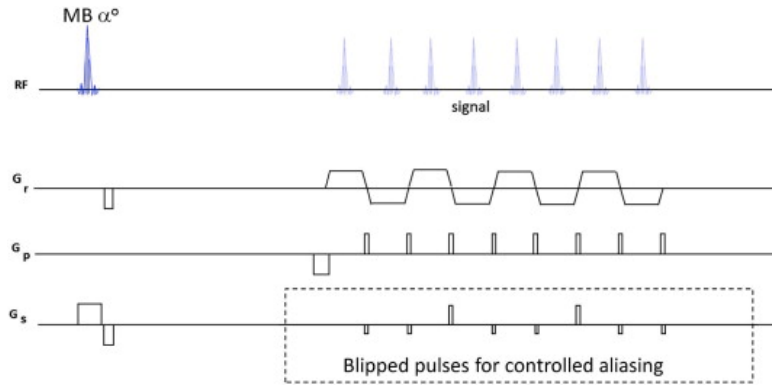


Figure 10: Simultaneous-multi-slice EPI with CAIPIRINHA shifting. Multiband pulse excited several slices at the same time and the additional blipped gradient pulses are applied to create inter-slice image shifts. The linear combination of their signals is acquired and unaliased by parallel imaging techniques. Figure shows the creation of an FOV/3 controlled aliasing achieved by application of 2 negative polarity blipped pulses followed by a 3rd positive polarity pulse of larger amplitude to null the gradient moment in the echo. (Reproduced from [71])

The SMS approach allows for the increase in the number of acquired slices, without having higher gradient demands. It can be further combined with k-space undersampling along the PE direction, resulting in a 2D acceleration. [66] The use of 2D SMS EPI for high-resolution fMRI was shown to be beneficial, allowing for substantial TR reduction without significant degradation in SNR or image quality [72].

2.4.2.3 3D echo-planar imaging

The 3D EPI sequence was for the first time suggested by Song et al. [73] and Mansfield et al. [2]. In this sequence, the same slab of tissue, being the whole volume of interest, is repeatedly excited and a k_x - k_y plane of k-space is acquired each time with a different k_z increment. As instead of slice selection the secondary phase encoding direction (along k_z) is used, when all k_z planes are acquired a 3D Fourier transform is applied to create a complete 3D image. Due to that, N_{slices} times more k-space points contribute to each image voxel leading to a 3D EPI's inherent SNR advantage given by a factor of $\sqrt{N_{\text{slices}}}$. On the other hand, because the time between subsequent excitations of the same tissue is much reduced, the steady state magnetization that is available for MR signal formation is decreased and so is the SNR.

In 3D EPI, the acceleration by PF and PI can be performed along both PE directions, therefore allowing skipping the entire k_x - k_y planes. The volume TR can be thus reduced by the factor of the fraction of non-acquired secondary PE steps (k_z -planes), making the 3D EPI substantially more time efficient than 2D EPI. Therefore it allows for higher spatial resolution within the same volume TR, or to reduce the measurement time. Although, the application of PI into two orthogonal PE dimensions leads to a considerable SNR losses, these losses are still smaller when the undersampling is spread out over the two PE dimensions,

than if it would be applied to a single one. However, the 2D SMS EPI shows smaller SNR losses triggered by the acceleration in the slice direction than the 3D EPI.

Generally, as during a long echo train of 3D EPI that is required to fully encode the volumetric information significant T_2^* decay occurs, the image quality of this sequence may be quite low. Moreover, the geometrical distortions due to long read-out period are present in two dimensions. However, the usage of segmented (multi-shot) excitation along with PI [74] can significantly reduce these problems as well as to increase the time between the subsequent excitations of the same tissue and therefore signal intensity. [66]

In fMRI, more important than SNR or tSNR is the effective functional sensitivity, which may be increasing even though the SNR decreases, if the effect of acquiring larger number observations over the same time outweighs the SNR losses. The higher functional sensitivity of highly accelerated 3D EPI protocol over their 2D variants was shown on both 7T and 3T, although having lower SNR, emphasizing the benefits of rapid sampling of the BOLD signal. [74] [75]

2.4.3 Nyquist ghost correction

Due to the EPI's inherent combination of high amplitudes and switching rates of gradients with long readout period the Nyquist ghosting artifact is very pronounced. To address this issue, different corrections can be used. First of all, the gradient coils should be designed in a way, so that the induced eddy currents would be minimized as can be achieved for example by their shielding. Since the EPI fills the k-space using the alternating trajectory, the exact timing between the signal sampling and application of readout gradients is critical, otherwise phase difference between lines collected in opposite direction, i.e. odd and even echoes, occurs. To minimize this error, the timing can be adjusted by setting sampling clocks or by adding appropriate phase shifts to the raw data. As the required phase shift (phase correction parameters) depends on the position along FE direction, i.e. position within a k_x line (x), their values along the whole line can be assembled to a vector. The determination of required phase correction parameters for ghost correction can be achieved by various methods of significantly different effectiveness. [63]

Global phase correction approach measures a reference scan with three "navigator" echoes, i.e. k_x lines ($\mathbf{S}_1^+, \mathbf{S}_2^-, \mathbf{S}_3^+$ - values of measured complex signal along the line, i.e. one value for each x are assembled to vector, therefore can be represented by a curve) acquired under alternating readout gradients ($\mathbf{G}_1^+, \mathbf{G}_2^-, \mathbf{G}_3^+$), however without application of phase-encoding gradient. Then, from the \mathbf{S}_1^+ and \mathbf{S}_3^+ the \mathbf{S}_2^+ is interpolated and the required phase correction parameters (\mathbf{R}) are determined separately for even and odd echoes by comparison

of measured \mathbf{S}_2^- and calculated \mathbf{S}_2^+ . Then, each line measured under \mathbf{G}^+ is phase corrected by the corresponding vector of phase correction parameters \mathbf{R}^+ and the linear measured under \mathbf{G}^- are phase corrected by corresponding \mathbf{R}^- vector. The correction is performed by their conjugate complex multiplication. The approach described corrects for the linear phase errors (depending on the x coordinate) of the measured data. Further, by cross-correlation of linearly phase corrected reference echoes, the constant phase shift between echoes measured under \mathbf{G}^+ and those measured under \mathbf{G}^- can be calculated. Then, the constant phase correction by removing this determined shift only from odd (or even) echoes is carried out. [76]

A more sophisticated local phase correction approach measures a reference scan with at least two echoes ($\mathbf{S}_1^+, \mathbf{S}_2^-$) acquired under readout gradients ($\mathbf{G}_1^+, \mathbf{G}_2^-$) without application of PE gradient. However, unlike in global approach the phase correction parameters are determined so that they characterize the curve of phase differences between the \mathbf{S}_1^+ and \mathbf{S}_2^- , i.e. they are determined depending on at least one correlation between them. For each position x a phase correction can be defined by multiple parameters given by the coefficients of phase-difference curve's power series in that position. Usually the coefficients of the 0th and 1st order of the power series are taken into consideration, therefore the constant and linear phase corrections are applied. Using higher orders, non-linearities in the phase difference curve can be taken into account. Since the curve of phase differences is smoother than the phase curves themselves, the phase correction parameters can be determined with higher precision and robustness. Further, their determination can be carried out per separate segments of phase difference curve, resulting is a more precise correction. Lastly, the weighting according to signal intensity combined with spatial weighting depending on a signal's position within MR image, allowing for high precision of phase correction in the image segment of interest. [77]

The use of both phase correction algorithms allows for reduction of Nyquist ghosting and it's application greatly improves image quality, particularly at higher field strengths where, due to increased magnetic field inhomogeneities and strength of eddy currents, this artefact becomes more pronounced. However, as we will show in this thesis, because of all the benefits of local phase correction algorithm it significantly outperforms the global approach.

2.4.4 Statistical analysis

In fMRI experiments, brain activation is identified by repeated measurement of the volume of interest during certain stimulation or resting conditions. As the fluctuations in the signal caused by activation itself are quite small (approximately 0.5-5%), the methods of statistical analysis have to be applied to

differentiate between the signal changes of interest and physiological and technical noise.

There are two main categories of fMRI analysis methods. Model-based correlation techniques such as the General Linear Model (GLM), require a priori knowledge of the time course of experimental stimulation and expected hemodynamic response. Model-free methods, in contrast, do not require any a priori knowledge, making them easier to use and also more suitable for the assessment of functional connectivity from resting-state fMRI data. The main representative of this group, Independent Component Analysis (ICA), is a computational technique allowing for identification of hidden statistically independent sources from multivariate data capable of a stand-alone assessment of brain activation. Since the ICA identifies signal sources based on spatial independence rather than the temporal similarity between stimulus and response, it was proposed to use ICA to distinguish between task-related activation and other, non-task-related components of fMRI signal [78].

In classical ICA, the decomposition of the data from the fMRI experiment consisting of n voxels measured at p distinct time points, which can be written as a $p \times n$ matrix X , is sought such that

$$X = AS. \quad (57)$$

The matrix S is optimized to contain statistically independent spatial maps in its rows, i.e. spatial areas in the brain, each with an internally consistent temporal dynamic, which is characterised by a time-course contained in the associated column of the square mixing matrix A .

This basic ICA analysis cannot be however used for fMRI data, as it does not include a noise model and therefore assumes the signal to be completely characterized by the estimated sources. Further, it assumes the square mixing matrix meaning that the signal is not constrained to be contained within a lower dimensional subspace. To address these issues, the probabilistic Independent Component Analysis (PICA) model [79] [80], which is used in FSL's tool MELODIC [81], that allows for a non-square mixing process and assumes that the data are confounded by additive Gaussian noise, has to be used for fMRI analysis. Similar to the noise-free case, the probabilistic ICA model can be defined by

$$X = AS + \mu + \eta, \quad (58)$$

with η representing the Gaussian noise and μ the mean of the observations X over the set of all voxels. The PICA model is similar to the standard GLM with the difference that, unlike the design matrix in the GLM, the a priori knowledge of mixing matrix A is no longer necessary, but it is estimated from the data as part of the model fitting. Further, the spatial source signals correspond to parameter estimates in the GLM, however being statistically independent. [81]

The main drawback of ICA for task fMRI is difficulty in interpreting the output, e.g. the need to identify the components reflecting task-relevant activation out of the many (up to few hundreds) generated. This is based on the presence of activation in the area corresponding to the stimulation paradigm, supported by their time-course consistency. However, it is capable of isolating activation in data containing stimulus-correlated motion and as well to differentiate the activation from the artefacts related Nyquist ghosting, and parallel imaging reconstruction errors. ICA has been shown to be able to isolate primary motor activation with only negligible contamination by motion from the heavily motion-contaminated fMRI data. Further, ICA was shown to have higher specificity and in the analysis of motion-contaminated data also higher sensitivity to activation than the GLM. [82]

3 Methods

3.1 Data acquisition

The aim of the measurements done in this study was twofold i) to provide the data to develop and test the phase combination methods and ii) to generate time-series EPI data that, using the final implemented combination method, can illustrate the potential of combined fMRI and QSM. The data for both i) and ii) were measured by a 7 Tesla MR whole body Siemens Magnetom scanner (Siemens Healthcare, Erlangen, Germany), using 32-channel head coil (Nova Medical, Wilmington, USA) consisting of a birdcage transceive coil and 32 receive elements.

The scans for i) were measured gradually, over the course of the development of the phase combination method initially scanning water filled MR phantom and later also volunteer. At first, low resolution single-volume data of small number of slices were measured by Siemens product 2D EPI sequence and used for fast testing and debugging during the course of method development. When the implemented reconstruction was working on this dataset, to check the correct performance in the case of multi-volume acquisition another dataset of several repetitions was measured by 2D EPI and to check the performance for the case of multi-echo acquisition, a double-echo GRE scan was acquired. Subsequently, the higher resolution (1.5mm) multi-volume (50) multi-slice (120) 2D EPI dataset was measured, to test the capability of implemented reconstruction to work with such a large datasets as needed for our purposes. Then to optimize the VRC combination for fMRI brain scans (e.g. choice of phase-matching point), a small, single-volume volunteer dataset was measured using general fMRI protocol. Finally, several datasets were measured by different EPI sequences (2D simultaneous-multi-slice (Minnesota, MGH), 3D EPI (Poser)) with already user pre-modified reconstruction pipelines (see Section 3.2.2), to check whether the VRC combination still performs correctly or whether additional modifications (e.g. shifting of VRC branch insertion) are required.

For ii) one high resolution multi-echo gradient-echo 3D scan with monopolar readout of total acquisition time of 7 min 42 secs, used as reference for QSM and further eight fMRI datasets, using 2D SMS EPI developed at CMRR (Minnesota) [70] and segmented 3D EPI sequences developed by Poser et al. [74], were measured with protocol details listed in Table 1. Since the basic Siemens 2D EPI sequence was for technical reasons not running when the data for ii) were acquired, the 2D SMS EPI sequence with multiband (MB) acceleration factor of 1 was used instead. For 2D SMS EPI MB factors ranging between 1 (i.e. only one

slice acquired at one time) and 4 were used. For 3D EPI, due to technical problems of the sequence the 3D acceleration factor was not used, only in-slice acceleration. Common to all measurement, axial orientation, as required for QSM analysis, and interleaved slice acquisition were used and the acquisitions were accelerated by the GRAPPA factor of 2 and partial Fourier factor of 6/8. The separate-channel data of all datasets were combined by the VRC approach, using the online reconstruction developed in this project as described in Section 3.2.2. Besides, to see whether the susceptibilities obtained by using TGV based QSM algorithm are influenced by the arbitrary phase offset introduced by VRC approach, the GRE scan was additionally combined by ASPIRE [46], which removes physical phase offsets (rather than relative phase offsets) completely.

The fMRI time-series data were measured both in a resting condition and during performance of a motor task. The block-designed finger tapping paradigm consisted of 7 rest and 6 movement phases of 24 s each, presented in an alternating design starting and ending with rest phase, was performed by dominant (right) hand. Visual cues specifying when to start and stop the movement were presented using the software Presentation (Neurobehavioral Systems, Albany, USA), which was triggered by the MRI scanner. In the task condition, a green circle on a black background was displayed, alternated by a red circle during the rest condition.

Protocol acronym	Voxel size [mm]	Matrix size	Interslc. gap [%]	rBW [Hz]	TR [ms]	TE [ms]	FA [°]	NR
3D GRE	0.36x0.36x0.9	576x576x112	20	380	22	6.3; 12.6	10	1
2D EPI MB1 (task)	1.64x1.64x3.0	128x128x30	20	1446	2000	25	70	156
2D EPI MB1 (rest)	1.64x1.64x3.0	128x128x30	20	1446	2000	25	70	156
2D EPI MB2 (task)	1.64x1.64x3.0	128x128x30	20	1446	1000	25	54	312
3D EPI (task)	1.48x1.48x1.5	128x128x80	-	1302	6248	25	16	52
2D EPI MB1	1.64x1.64x3.0	128x128x30	20	1446	2000	25	70	1
2D EPI MB2	1.64x1.64x3.0	128x128x30	20	1446	1000	25	54	1
2D EPI MB3	1.64x1.64x3.0	128x128x30	20	1446	600	25	43	1
2D EPI MB4	1.64x1.64x3.0	128x128x28	20	1446	400	25	36	1

Table 1: Acquisition parameters of measured data. Further parameters common to all data were: GRAPPA = 2, interleaved slice acquisition and axial orientation. EPI data were acquired with PF = 6/8.

3.2 VRC implementation

3.2.1 Offline (in MATLAB)

Since the debugging and implementation itself is much easier in MATLAB than in ICE, at first the evaluation of using different virtual receiver coil images for VRC approach was performed in offline reconstructions using and modifying an existing MATLAB implementation of the VRC approach. Before the offline reconstruction was carried out, the export of uncombined separate-channel phase and magnitude DICOM image files from the MR scanner, followed by the conversion to NIfTI format [83] by the MATLAB tool “Siemens DICOM sort and convert to NIfTI [84]” was required. As during fMRI run up to hundreds of volumes are acquired, the size of uncombined data of single run is usually in order of gigabytes. This makes the offline combination very time-consuming, even though the VRC approach itself is not very computationally demanding.

The combination qualities achieved by VRC approach when using VRC images obtained by different methods were compared. For all approaches the ROI_M , out of which the voxel of maximal summed intensity used for phase centering is chosen, was restricted to 1/20 of the FOV in the xy-plane and to 1/4 of the FOV in the z-direction. The considered methods were: original Scalar Phase Matching (SPM), magnitude-weighted SPM (mwSPM) and two additional methods to which will refer as separate slice SPM and separate channel SPM.

In the separate slice SPM approach, the creation of a virtual reference coil image is done for each slice separately. That means that for each slice the VRC center localized in the restricted FOV (only in xy-plane) is determined. Subsequently, the phase of each channel of certain slice is centered and the VRC image is created slice by slice. For this method, the Gaussian smoothing of relative phase offsets with 10 mm sigma was done in 2D, unlike for all other methods where 3D smoothing with the same sigma was applied. Compared to all other considered methods, the implementation of this approach on the MR scanner would be much easier, since in the default ICE reconstruction pipeline the measured data are processed slice by slice. The other approaches require simultaneous access to all slices during the process of VRC image creation, and therefore in ICE, their accumulation is required, what both slows down the reconstruction and increase the computational demands.

The separate channel approach chooses different phase-matching point for each coil based on its maximal signal intensity within the ROI_M . Therefore the intensity of the chosen phase-matching point should be in all channels sufficient and hence the phase in that point should be reliably defined. The phase of each

channel is then nulled at potentially different voxel and the VRC image (the whole 3D volume at the same time) is created by their combination.

The SPM and mwSPM approaches for VRC image creation were implemented as described in Section 2.2.5.

3.2.2 Online (in the Siemens Image Calculation Environment)

As a part of this thesis, the phase combination by VRC method was implemented into the Image Calculation Environment (ICE) (C++ framework) to run on the Siemens scanner's reconstruction computer. Thanks to that, the phase combination can be performed directly on the scanner, during the data acquisition itself (or afterwards by retro-reconstruction) followed by export of the combined data only. Therefore, the reduction of the data amount necessary to export by the factor of a number of channels of the used coil was achieved. However, further reduction by the factor of measured slices is possible, as the combined data can be displayed in so-called Mosaic format, where all slices of one volume are displayed next to each other in one large image. In total, the reduction of data amount which needs to be exported by the factor of $2 \cdot NR \cdot N_{chan} \cdot N_{slc}$ can be thus achieved, where the factor of 2 is caused by the export of both magnitude and phase and NR represents the repetition number, i.e. the number of volumes acquired within a run.

A data processing pipeline created by ICE program, consists of several so-called "functors" each of which performs a certain part of reconstruction. They work sequentially one after another and are further arranged into so-called pipe services that are responsible for the coordination of processes. The user can otherwise create completely new reconstruction pipeline, or modify the default reconstruction pipeline released by Siemens. The raw data starts to be reconstructed directly after it is measured and goes through the whole pipeline, while subsequent data are still being acquired. The VRC combination is implemented by creating several functors, each performing certain encapsulated part of the reconstruction. After Fourier transformation, the default reconstruction pipeline of used sequence is bifurcated and a separate branch performing the VRC combination is introduced. The original branch and therefore the original image series are left unmodified and separate series of magnitude and phase images combined by VRC approach are created. Further, for direct evaluation of the achieved phase-matching quality, image series of Q-maps is created.

The VRC's branch is inserted after FT (splitting done by BranchingFunctor), therefore it receives already the slice data, coming one after another. Due to the best performance quality, as we will show later, the approach using VRC image created by magnitude weighted SPM was implemented. The final part of processing pipeline, where the VRC phase-combination is inserted is shown in

Figure 11. Since this approach requires simultaneous access to all slices they all have to be accumulated (done by SliceAccuFuncutor) to create the whole volume, out of which the VRC image and subsequently the differences between individual channels and VRC image, i.e. relative phase offsets, are calculated (by VrcPoCalculatorFuncutor). During that, the whole pipeline has to be stopped (SleepingFuncutor) since otherwise the following functors, requiring the knowledge of relative phase offsets would not work properly. The VRC image is created only for the first volume (and only for the first echo in the case of multi-echo data) of a measurement (chosen by SelectorFuncutor), and removed for all subsequent volumes (PoRemovalFuncutor), significantly reducing the reconstruction time if many volumes are being measured, as in the case of fMRI. The phase-matched data are then combined using magnitude-weighted approach and the Q-maps are calculated. Finally the combined magnitude and phase images are extracted out of combined complex data (FinalizingFuncutor) and send back to the default pipeline, however skipping the functors that perform the original combination (adaptive combine or sum-of-squares). The imafinish functor fills image header parameters and the images are sent to the Patient Browser for displaying.

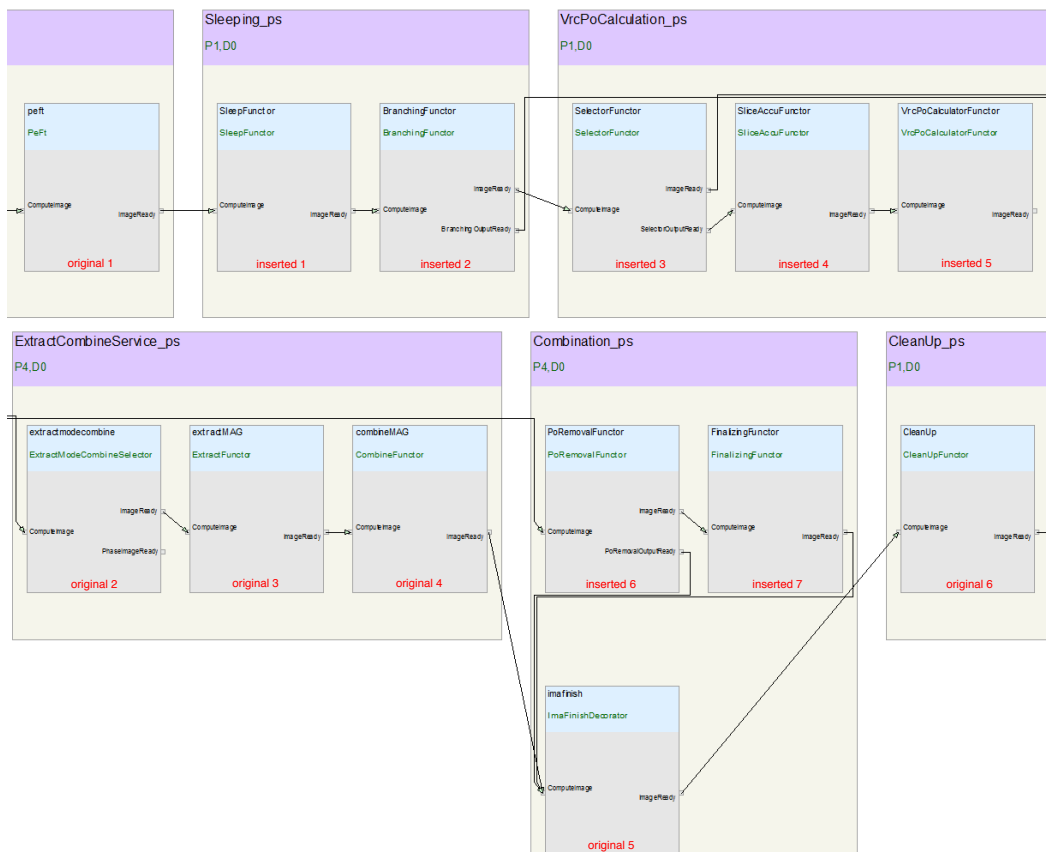


Figure 11: The final part of processing pipeline for VRC phase-combination created by ICE program. Note that the VRC functors are inserted into default branch after Fourier transformation (peft) and that the output of the default reconstruction pipeline is left unmodified.

4 Analysis

4.1 Evaluation of VRC combination

VRC combined images were visually inspected and checked for any evident errors. In the case of phase images, no open-ended fringe lines should be present in the areas of sufficient signal intensities. The inspection of undesirable phase jumps between slices was performed and the sufficient phase-matching quality depicted by a Q-map was verified. The magnitude images were checked for any visible signal dropouts, caused by a complex signal cancelation, therefore representing the points where the phases between channels of phase-array coil were not matched and led to a destructive interference.

4.2 fMRI analysis

The analysis of the BOLD signal changes during fMRI time-series was performed on magnitude data by using FSL tool MELODIC [85]. This tool uses Independent Component Analysis for decomposition of a 4D data set into different spatial and temporal components. For the runs with task, by visual inspection of all components, those representing the task-related activation were assessed based on time-course agreement with stimulation paradigm and spatial localization in the motoric area. For the runs with resting-condition, the IC's components representing default brain networks were assessed.

Before the fMRI analysis itself, the motion correction of the whole time-series to the middle volume was carried out by FSL tool MCFLIRT [86], which performs a rigid-body co-registration by using normalized correlation cost function and trilinear interpolation. However, to test the ICA robustness even in the case of motion-contaminated data, the ICA was for one fMRI run performed on the not motion-corrected data as well.

4.3 QSM analysis

The aim of this thesis was to demonstrate the possibility of generating QSM images from a rapid series of quite low resolution EPI data measured under task or resting-state condition. The susceptibility maps were generated by iterative QSM algorithm based on the TGV [5], using the default parameters of 1000 iterations and TGV-regularization parameter ratio equal to 3 ($\alpha_1/\alpha_0 = 0.0015/0.0005$). For the quantitative comparison of obtained QSM values, 12 regions of interest (ROIs) located in the deep grey matter structures were defined

based on the GE QSMs, with the details listed in Table 2. Then the mean susceptibility over each of them was calculated and compared between individual QSMs of interest by paired t-test.

Region acronym	Localization	Spatial extent [voxels in GRE]
ROI 1	Red nucleus left	224
ROI 2	Red nucleus right	208
ROI 3	Substantia nigra left	61
ROI 4	Putamen left	94
ROI 5	Globus Palidus right	97
ROI 6	Globus Palidus left	150
ROI 7	Substantia nigra right	50
ROI 8	Putamen right	97
ROI 9	Putamen left	70
ROI 10	Globus Palidus right	70
ROI 11	Caudatus right	73
ROI 12	Caudatus left	56

Table 2: Details of defined regions of interest.

For fMRI runs, out of each volume a separate QSM was generated and subsequently motion corrected (MC) to the middle volume of the run. Then the average susceptibility maps over the time-series of MC QSMs acquired by 2D SMS EPI and 3D EPI sequences with different protocol parameters were calculated and compared (both qualitatively and quantitatively) with those generated from the second echo, i.e. with TE closer to EPI, of the “gold standard” high resolution gradient-echo 3D scan combined by ASPIRE approach.

To check whether the susceptibility values obtained by this algorithm depend on the phase combination method (e.g. influence of by the arbitrary phase offset introduced by VRC method), the QSMs generated out of the same GRE scan however combined by VRC or ASPIRE approach respectively were compared. Furthermore, to observe the effect of using different echo times, the QSMs reconstructed from both echoes of GRE data were compared. Since the echo-times in EPI are often different than in GRE (e.g. in our study 4x, resp. 2x longer), this effect might then potentially lead to discrepancies in their QSMs.

To observe the effect of motion correction on the QSM analysis, the over-run average QSM was also calculated from the not MC QSMs and compared with average of MC QSMs. Further, the average of MC QSMs was compared with QSM from a single, middle volume of the run (reference volume for MC). To study the effect of BOLD changes, heartbeat, respiration and other physiological and non-physiological effects on QSM values, the motion-corrected QSMs were analysed by ICA, i.e. the functional QSM analysis was performed. Moreover, the

over-run standard deviation image of the MC QSMs of task condition was compared with that from the resting condition.

Since QSM analysis is computationally expensive, instead of calculating QSM for each volume and averaging them, the over-run average magnitude and phase could be calculated and used for creating average QSM, when the time-course of the QSM is of interest. In this case only a single QSM analysis is required and the computational time is decreased by approximately the number of repetitions. Although the computational expenses of this approach are much lower, it can be used just in case when the time variation of QSM is not of interest. The required steps are shown in Figure 12. Before the average magnitude and phase over the run were calculated, their motion correction to the middle volume was performed. However, the direct MC of wrapped phase images is not possible, as the inherent MC's interpolation would result in an averaging over the wraps. Because of that, the MC was carried out in complex space, i.e. by separate MC of the real and imaginary part. The parameters for motion correction were calculated from the magnitude time series and then applied separately to real and imaginary parts of the raw data. Out of them, the MC magnitude and phase were calculated, averaged over run and used for QSM analysis. This approach for calculating the over-run average QSM was compared with the one that averages the QSMs of individual volumes.

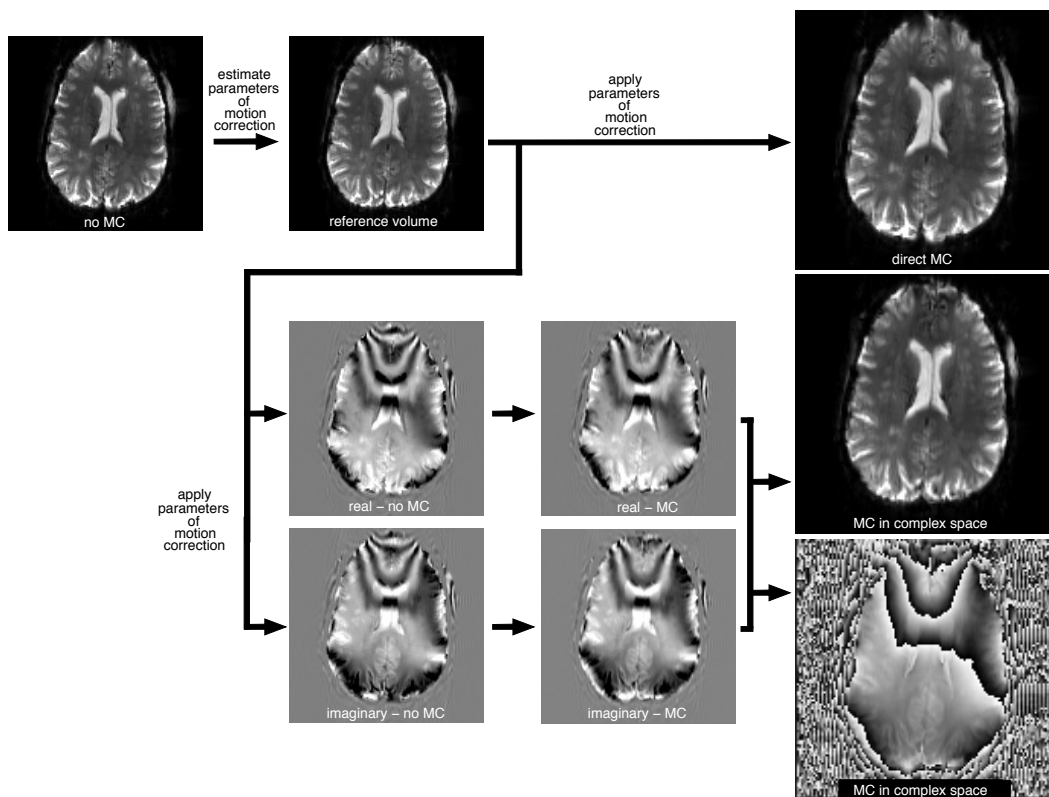


Figure 12: The steps required for motion correction of phase, i.e. for the MC in complex space. The parameters for MC of real and imaginary parts are retrieved from the MC of magnitude.

5 Results

5.1 VRC performance

In a first step, the performance of VRC combination when using different VRC images was studied. As Figure 13 shows, when the VRC image was created by separate slice SPM, although almost perfect phase matching in the final combination was achieved (Q-map of combined), the phase discontinuities between slices occurred. As the Q-map for VRC image shows, although the phase matching in the center of each slice was almost perfect, it drops down away from the ROI_M as typical for SPM approach. In the separate channel SPM, the VRC image showed very low combination quality even in its center, caused by destructive interference between the signals of individual channels, which were all centered to a different voxel. This was accompanied by significant losses in SNR in magnitude image and in phase-matching quality of the final combination and the combined phase thus contained open-ended fringe lines. Although SPM combination allowed for almost perfect combination with only very small quality reduction in the posterior area and close to the ventricles, the VRC image showed significant decrease of quality Q away the ROI_M . The use of magnitude-weighted SPM for VRC image creation was shown to outperform the original SPM approach. The combination quality of VRC image was greatly increased even in the areas more distant from ROI_M . The usage of mwSPM for VRC image creation thus allowed for very high combination quality over the whole brain, therefore yielding combined images with higher SNR than all other considered methods.

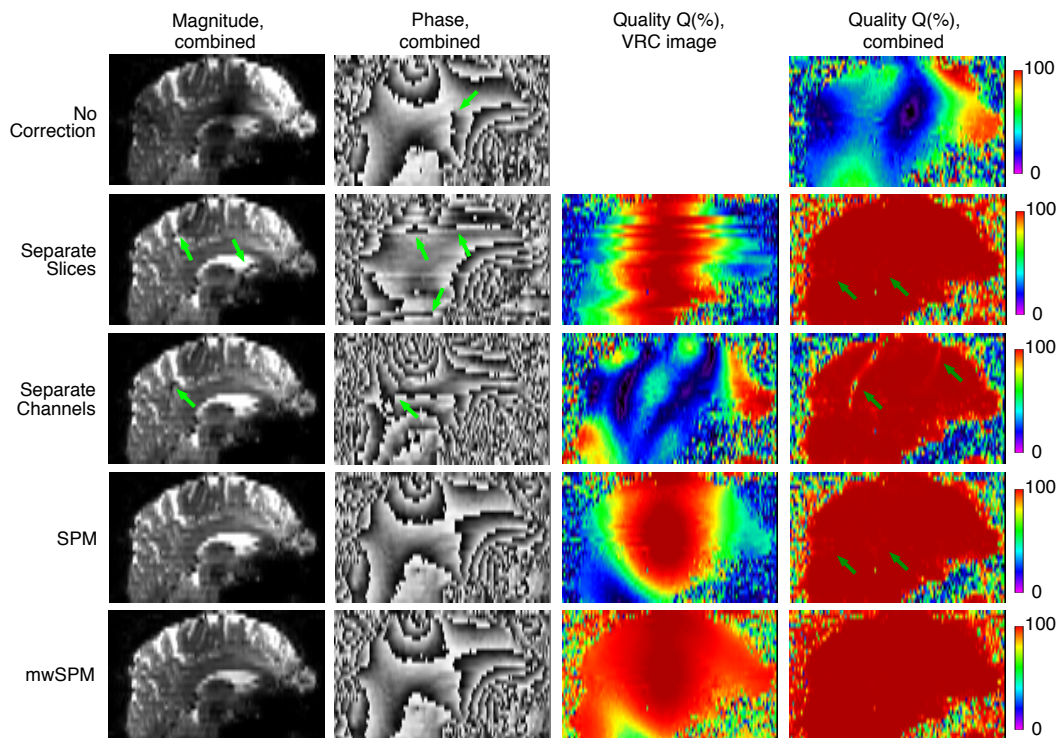


Figure 13: The comparison of VRC phase-combination of EPI data using different VRC images. Using both general SPM and mwSPM VRC image allows for high combination quality without any evident phase errors. However, as is visible from Q -maps of VRC image, the mwSPM image reaches higher Q values even in the areas further away from ROI_M . Separate slice and separate channel approaches show decreased combination quality and create visible errors (phase discontinuities, signal dropouts) as marked with arrows.

The histograms of the Q -values in Figure 14 are shown in semilogarithmic scale, and compare the VRC image combination quality of individual approaches in the brain voxels only. The separate channel SPM approach, in which each channel was centered to a different voxel, i.e. to a different phase, showed very low phase-matching quality. The separate slice SPM approach showed larger number of highly matched voxels than the original SPM method, as the almost perfect phase matching was achieved in the center of each slice, rather than in the center of the volume. However, as showed in Figure 13, this resulted in the phase inconsistencies between the slices. The mwSPM VRC image achieved the largest number of voxels with high combination quality, since even the voxels distant from ROI_M were highly matched.

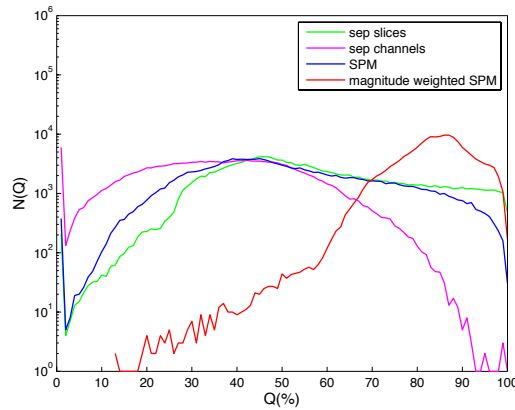


Figure 14: The comparison of the histograms of Q -values for considered VRC images. For this analysis, only the in-brain voxels were used. The mwSPM approach achieves the largest number of highly matched voxels. Note the logarithmic scale on vertical axis.

The histograms of the Q -values for the final combination are shown in Figure 15. When using VRC image created by separate channel method, the voxels with very low combination quality were present. Common Q -values were achieved using separate slice and SPM VRC images. The use of mwSPM VRC image allowed for very high Q -values in most of voxels and only very small number of voxels with low combination quality.

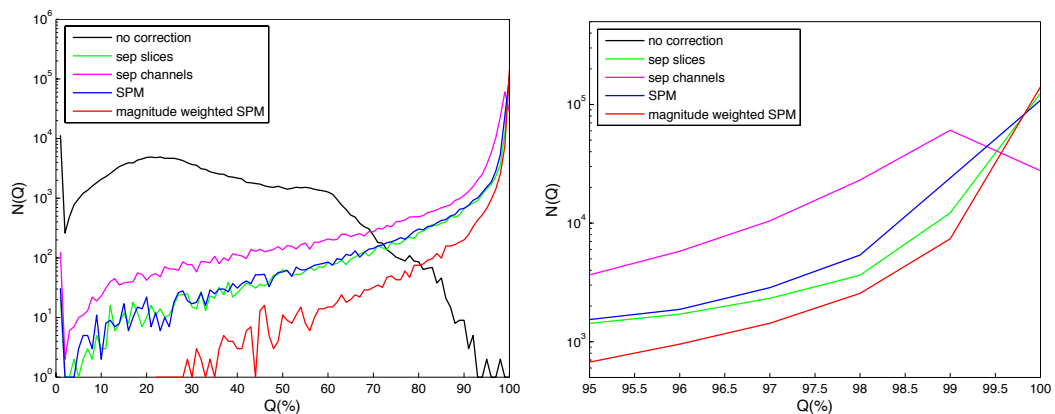


Figure 15: The comparison of the histograms of Q -values for the VRC phase-combination of EPI data using different VRC images. For this analysis, only the in-brain voxels were used. The mwSPM approach achieves the best combination quality. Note the logarithmic scale on vertical axis.

In the second step, the optimization of ICE implemented VRC was required to consistently perform high-quality phase combination also for the quite low quality EPI data without further user interaction. As the most significant parameters, the choice of phase-matching point and the reduction of severe ghosting artifacts inherent to the EPI sequence were assessed. Figure 16 shows the significant increase of ghosting artifacts that occur when the local phase correction is not used, but instead the global correction is applied. This resulted in reduced phase-matching quality of both VRC image and of final combination and

in the creation of open-ended fringe lines in the combined phase. Since the brain scans are usually centred, the middle of the image often contains ventricles and large veins, i.e. areas where the phase might not be reliably defined. The definition of the slightly off-centred ROI_M (matching region of interest) and the choice of the point with the maximal summed magnitude over channels turned up to be the most optimal. Figure 16 shows the decrease in the combination quality caused by the definition of centered ROI_M, resulting in a choice of a phase-matching point in a ventricle, with the phase influenced by uncompensated flow, therefore leading to an error in estimating the phase offsets. The significant drop in the VRC image Q-values was observed, causing complex signal cancelation during the final combination. The optimized approach combining both of these parameters enabled for excellent phase-matching quality with high consistency, as depicted in Figure 16 and Figure 18, even for the low quality 2D EPI data.

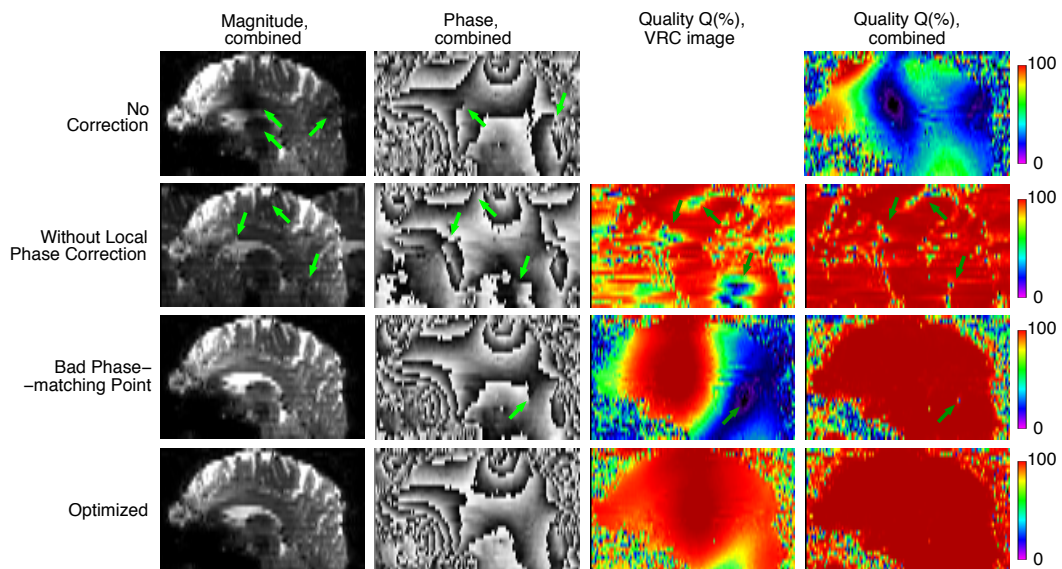


Figure 16: The comparison of VRC phase-combination of EPI data using different implementations. When using global phase correction approach (instead of local) or a phase-matching point with unreliably defined phase, the combination quality of both VRC image and final combination is decreased (see two middle rows). The visible errors (signal dropouts, open-ended fringe lines) are marked with arrows. The optimized set-up achieves very high Q-values over the entire brain.

The comparison of the histograms of VRC image Q-values for different implementations in Figure 17 is shown in semilogarithmic scale and for the brain voxels only. Surprisingly, the VRC image created when only the global phase correction was applied showed beside the great number of voxels with very low Q-values also many voxels with very high Q-values, however, as visible in Figure 16, these were distributed over the brain quite randomly. The use of matching point with unreliably defined phase caused significant decrease in the combination quality.

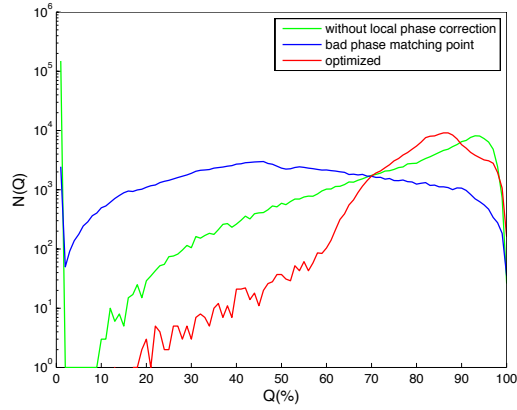


Figure 17: The comparison of the histograms of VRC images Q -values using different implementations. For this analysis, only the in-brain voxels were used. Beside the optimized set-up, also for the implementation using global phase correction has most of the voxels combined with very high quality. Note the logarithmic scale on vertical axis.

Figure 18 shows the histograms of the Q -values for the final combination. When only the global phase correction was applied, great number of voxels with very low combination quality was present. The optimized set-up achieved very high Q -values in most of the voxels and only very few voxels with low Q -values.

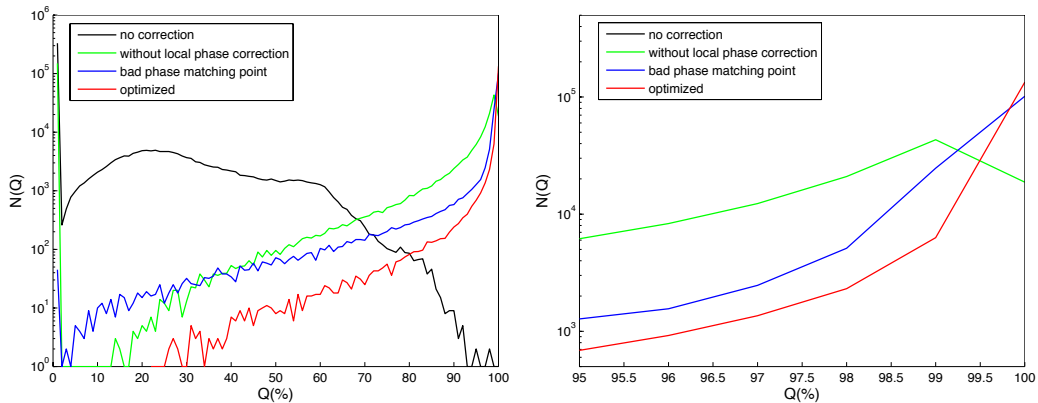


Figure 18: The comparison of the histograms of Q -values for the VRC phase-combination of EPI data using different implementations. For this analysis, only the in-brain voxels were used. The optimized set-up (i.e. using global phase correction and reliably defined phase-matching point) has most of the voxels combined with very high quality and only few voxel with lower Q -values. Note the logarithmic scale on vertical axis.

Further the effects of using 3D EPI sampling or MB acceleration on the measured uncombined phase and hence on the phase combination were studied. Although the 3D EPI data measured by the sequence developed by Poser et al. [Poser] showed higher noise content, no special artefacts in the phase data were observed. The 2D simultaneous multi-slice EPI data were measured by the sequence developed at CMRR, Minnesota with the MB acceleration factor ranging between 1 and 4. As Figure 19 shows, no phase jumps between slices or any other negative effects of the acceleration in the slice direction were observed, not even when the higher MB factor was used. In all data measured in this study, the VRC thus allowed for high-quality phase combination.

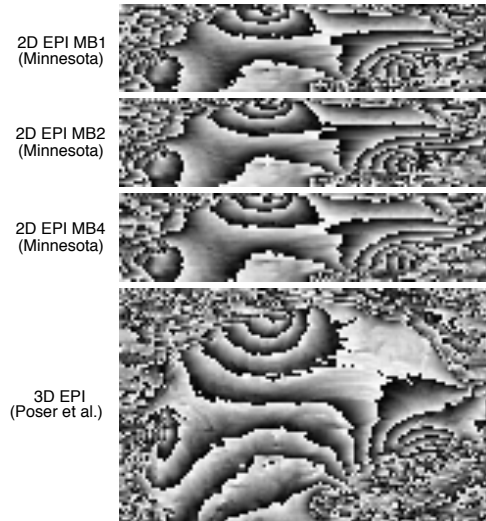


Figure 19: The phase of combined 2D EPI, 2D SMS EPI (Minnesota) and 3D EPI data. No odd phase effects (e.g. phase jumps) caused by multiband acceleration or 3D acquisition are present.

However, in a prior preliminary analysis by our group, when the 2D SMS EPI were measured by the sequence developed at MGH, Massachusetts with MB acceleration factor of 2 and combined by COMPOSER method, phase jumps between slices were observed. Similar results were obtained when their combination was carried out by VRC as shown in Figure 20. When a MB factor of 2 was used, the phase discontinuity between the bottom and upper half of the slices was observed. Beside that also the phase jumps between each of the slices in the upper half occurred. The pattern of phase jumps was also visible in the VRC image and in the unsmoothed phase offsets of individual coils. However, this pattern was smeared during the smoothing and thus it was not removed during the phase offsets' subtraction.

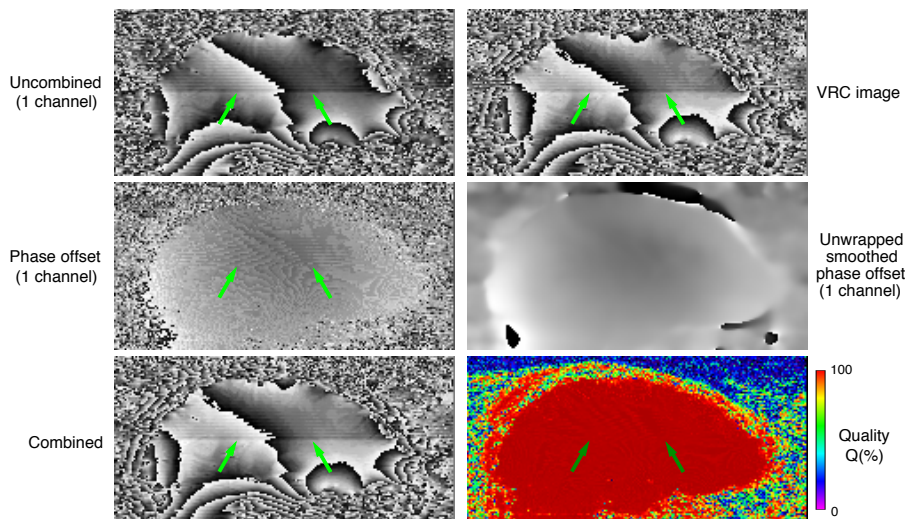


Figure 20: The combination of 2D SMS EPI data measured by MGH (Massachusetts) sequence using MB factor of 2. The combined data shows over-slice phase jumps. This pattern is also visible in the uncombined data and phase offsets, as well as in the VRC image. The overall combination quality is thereby decreased.

5.2 fMRI analysis

The ICA analysis on the magnitude data of all measured fMRI time series was carried out and the identification of all independent components and their corresponding timecourses was performed. The identified components overlaid on the corresponding magnitude images and their timecourses given in the form of normalized responses are shown in Figure 21. Due to the TR differences of individual EPI sequences, the smoothness of the timecourses was diverse (timecourses of subfigures 1, 2 and 3), however since the block-designed task was used, the identification of the task-related activation in the motoric area was possible in all cases (ICA components of subfigures 1, 2 and 3). The visible shift in the 3D EPI data activation compared to 2D EPI (depicted by blue arrow between the timecourses of subfigures 2 and 3) was caused by sooner start of stimulation paradigm due to the experimental error. The ICA was shown to be capable of identifying task-related activation even when applied to not motion-corrected data (subfigure 4), proving its robustness against motion. Further, even though the visual cues displayed during the task runs were very similar for the on (green circle on a black background) and off (red circle on a black background), the activation in the visual cortex with the matching timecourse was visible (subfigure 5). For the run of resting condition, the IC representing one of the resting state networks was assessed (subfigure 7). Another resting state network, one of those that stay active also when the resting condition is violated, was also observable during task run (subfigure 6).

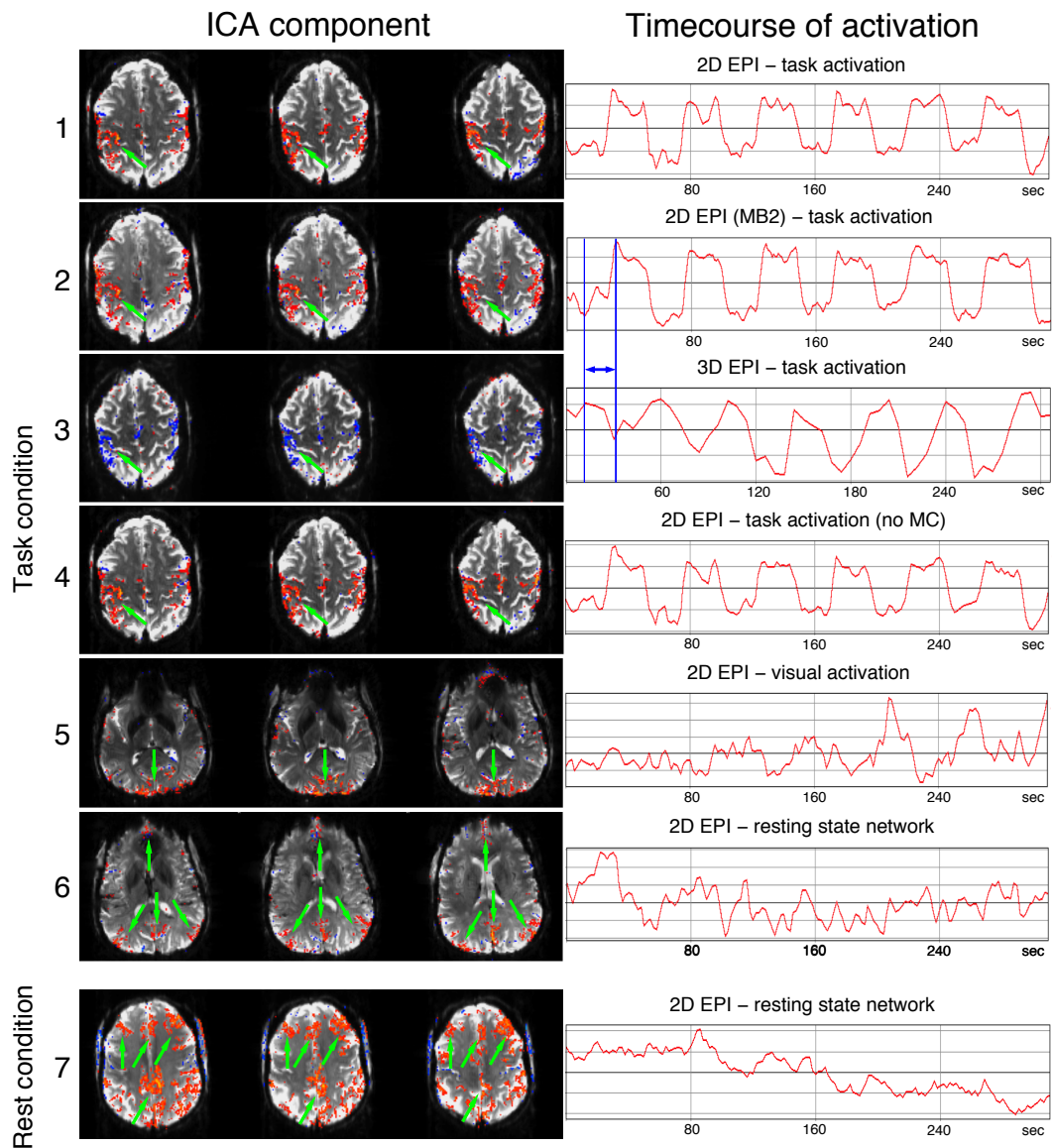


Figure 21: The activation maps and corresponding timecourses retrieved by ICA analysis of fMRI data. The timecourses of the task-related activations in the motoric and visual centers clearly correspond to the blocked task design (24 s on, 24 s off, starting with an off block). The IC components representing the activation of resting state networks are assessed by using previous knowledge of their localization.

5.3 QSM analysis

Figure 22 presents the qualitative comparison between the QSM generated from the second echo of reference high resolution GRE scan and the average QSMs generated out of a rapid series of quite low resolution EPI data measured with different protocols. Further it shows the corresponding single volume phase and magnitude data. As depicted, the used second order TGV-based algorithm allowed for creation of smooth susceptibility maps without any severe streaking or staircase artifacts in all cases. The GRE QSM showed great contrast between the iron-rich structures and surrounding tissue and allowed to differentiate

between the structures such as putamen and globus pallidus or small veins and surrounding, that was not possible in the EPI QSMs. Compared to EPI, the GRE phase was smoother and contained less wraps. Although both QSM and magnitude images of the EPI were more blurry, since the iron-rich deep grey matter structures were strongly hyperintense, their clear differentiation from the surrounding tissues was possible. However, the susceptibility values obtained from EPI data were different than those of "gold standard" GRE. The more pronounced signal decay that occurs during long readout period of EPI resulted in geometrical distortions and signal losses in the frontal regions. Therefore, the eroded brain masks of 2D EPI on which the QSM were calculated were cut-off in those regions, precluding the calculation of susceptibility in there. Although the 3D EPI data were more noisy, their signal intensity in those frontal regions was higher, resulting in less eroded masks and QSMs.

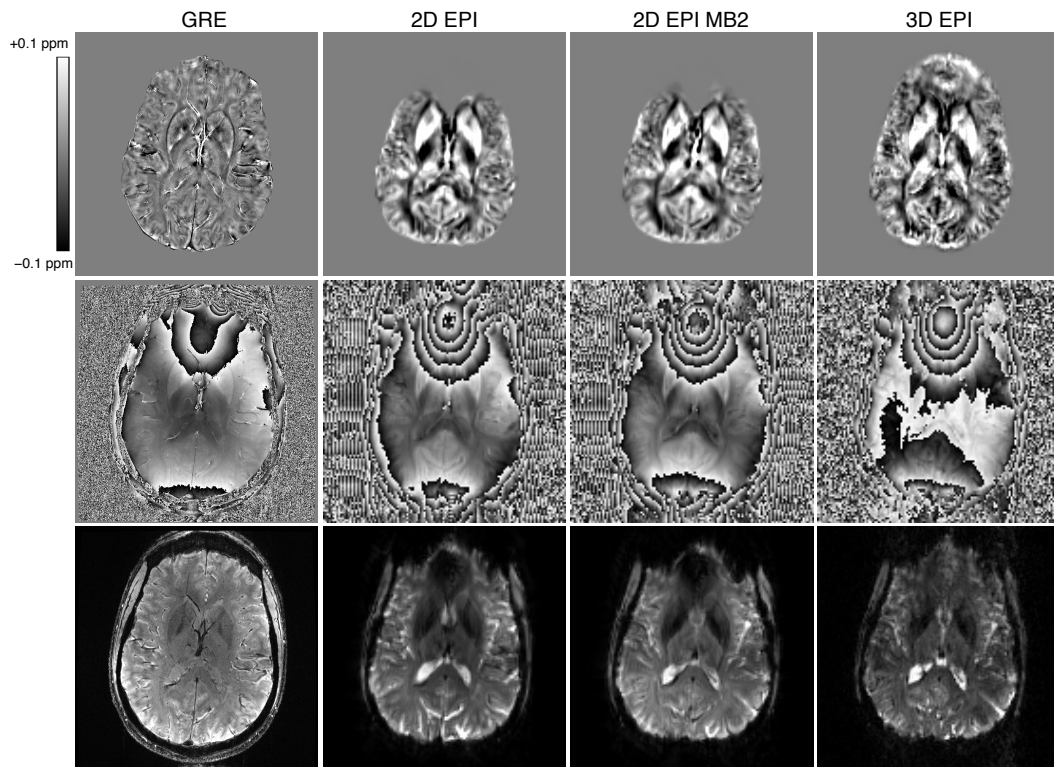


Figure 22: A qualitative comparison between QSM analysis results of the data measured using different sequences. The EPI QSMs provides different susceptibility values than GRE QSM. The EPI data are more blurry and shows significant geometrical distortions. In the frontal regions, the EPI's phase is more wrapped and the magnitude signal is decreased, resulting in QSMs masking out.

Figure 23 depicts a quantitative comparison of the mean susceptibilities over 8 of the defined ROIs, since due to distortions in EPI scans, the other were located partially out of the area of interest. The use of EPI data led to overestimation of the susceptibility values in most of the cases and also to their larger variance over the ROIs. The significant difference ($p=0.1213$) between QSM values obtained from the reference GRE data and from the EPI data. Although the mean

susceptibilities estimated by different EPI sequences were much more similar to each other than to GRE, they still significantly differed. Between the values obtained from 2D EPI MB1 and 2D EPI MB2 slightly less significant difference was observed ($p=0.8135$) then for the 2D EPI versus 3D EPI ($p=0.7866$ for MB1 and $p=0.6042$ for MB2).

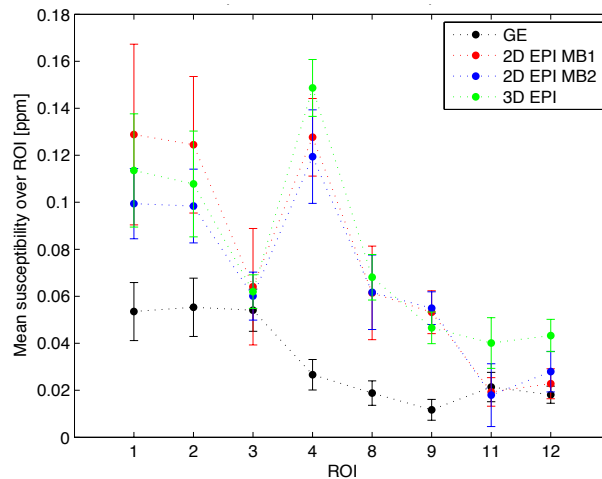


Figure 23: The mean susceptibilities over individual ROIs. Note the overestimation by EPI compared to "gold standard" GRE data.

Using the GRE data, the evaluation of echo time and combination method influence was done simultaneously by ANOVA. As Figure 24 shows, although the variance of the susceptibilities in the individual ROIs was quite large (usually around 25% of the mean value), the mean susceptibilities of all methods were very similar, i.e. in the range of 1 standard deviation in all ROIs beside 2. In these two ROIs, the difference between the two echoes was observed when combined by VRC, but not when with ASPIRE. In summary, no significant influence ($p=0.9996$) of used echo-time or combination method between the means over all ROIs located in deep grey matter structures was observed.

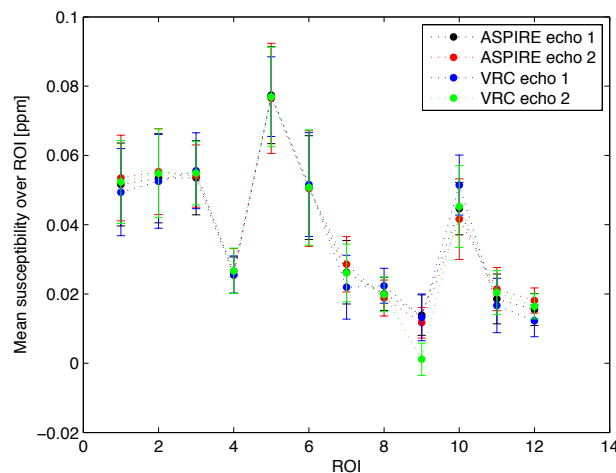


Figure 24: The mean susceptibilities over individual ROIs. Note the high similarity of mean values in all ROIs obtained from first/second echo of VRC/ASPIRE combined GRE data.

However, presented in Figure 25, due to the more pronounced dephasing of spins at longer echo time and hence the better phase contrast, the QSM of second echo showed improved contrast between intracortical veins and between GM and WM. Moreover, thanks to the resulting more accurate estimation of field maps, the noise levels as well as the streaking artefacts (mostly pronounced around the veins, due to the high susceptibility difference) were for the second echo reduced. On the other hand, the areas affected by strong field inhomogeneities, e.g. showed higher quality in the first echo QSM. Furthermore, due to the lower SNR of second echo in those areas, its brain mask used for QSM analysis and hence the QSM itself was slightly more eroded.

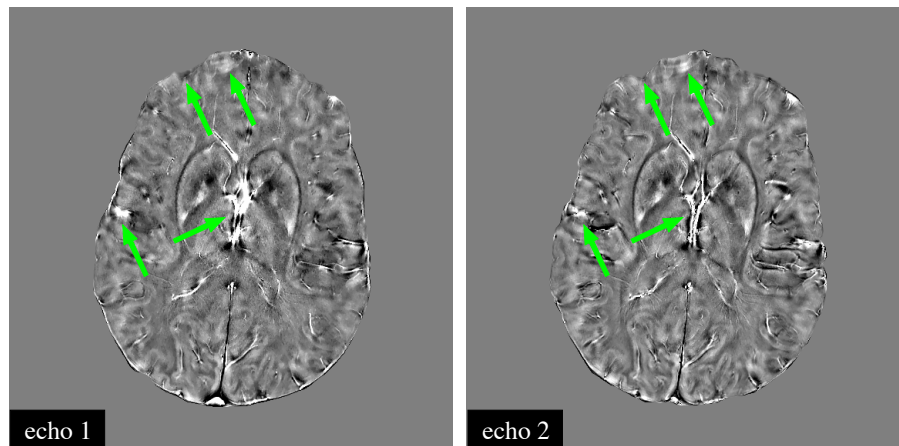


Figure 25: The QSMs obtained from the GRE data. The first echo is less eroded and shows higher quality in the frontal regions of high susceptibility differences. The second echo shows improved vein contrast and less streaking artefacts.

Figure 26 compares the over-run average QSMs and the standard deviation maps of task and resting run and shows the effect of motion correction. Due to larger over-run variance of resting data, these average QSMs were more blurred. Although this variance was reduced by motion correction, because of the averaging introduced by this process, the quality of the QSM was not markedly improved. The larger effect of motion correction on the resting data was caused by the larger movements (cumulative rotation around y-axis of 1.8° compared to 0.2° of the task run) that often occur when the subject is not focused on the task performance. The large variance of resting QSMs even after motion correction might be caused by the orientation dependency of QSM analysis, which cannot be corrected by simple MC. The task QSMs varied mostly in the areas of low signal intensities (e.g. veins, frontal area, sagittal sulcus) and did not show any direct effect of the task performance.

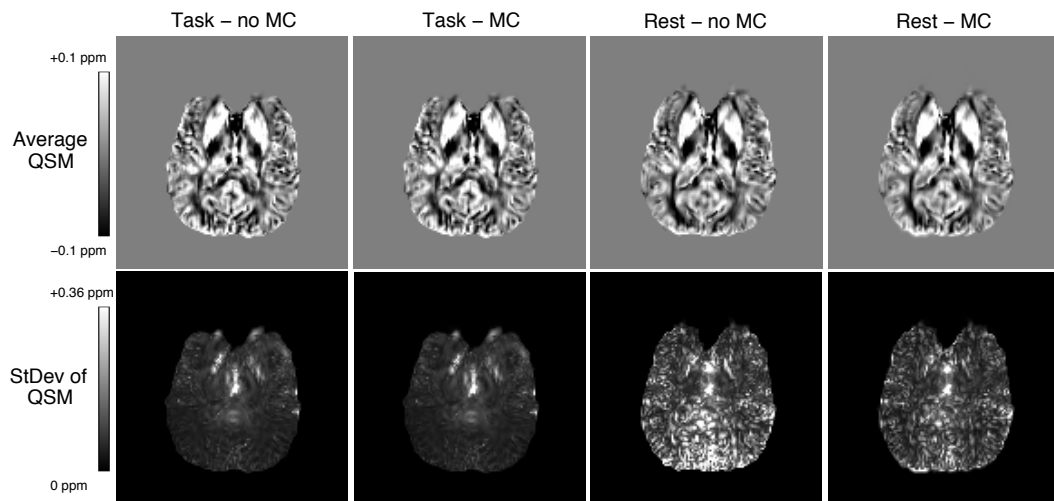


Figure 26: The comparison between the average QSMs and standard deviation maps of the task and resting runs. Beside the higher motion during resting run, and thereby more pronounced effect of motion correction, no other differences are visible.

The functional QSM analysis by ICA also did not show any clear, task related activation. However, a component suspected to represent the changes related to breathing was determined. As Figure 27 shows, it was localized mainly in the sagittal sinus and its main frequency was about 1 per 9 seconds as visible from the timecourse and powerspectrum diagrams. The powerspectrum analysis showed presence of the harmonic frequencies. To reduce the effects of physiological noise, a bandpass filtered version of the QSM time series was generated with cut-off values of 0.08 Hz and 0.60 Hz. Task-related activation components were also not observable in this filtered data.

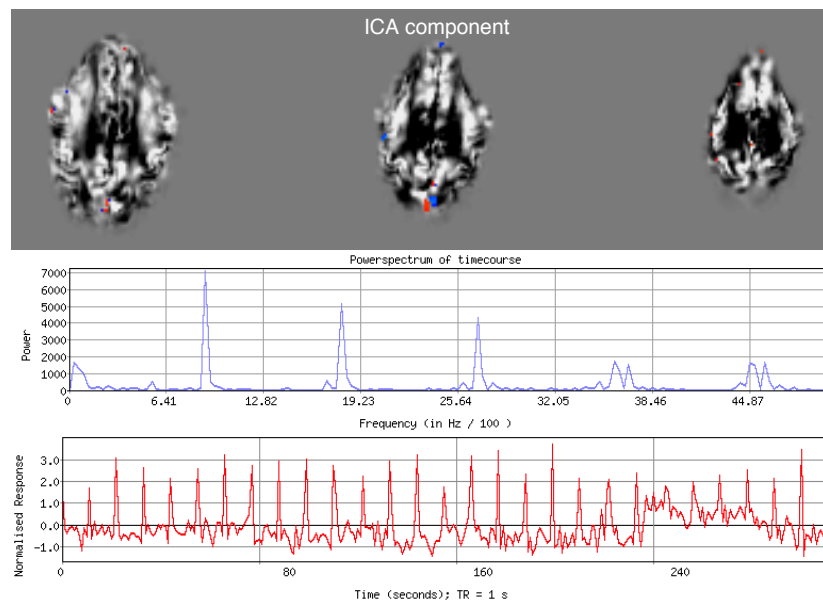


Figure 27: The oscillating component of functional QSM analysis localized in sagittal sinus retrieved by ICA, suspected to represent the changes related to breathing.

Figure 28 shows a comparison between a single volume of QSM time-course and the average QSM. As expected, the higher SNR of the averaged data resulted in a higher quality of the average QSM. This effect was more pronounced for the 3D EPI data, due to their higher noise content.

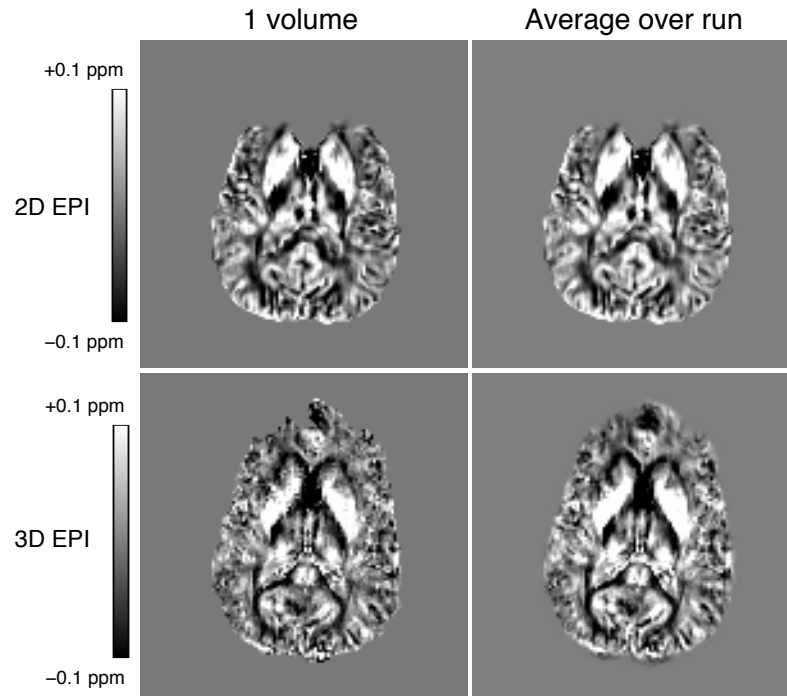


Figure 28: The comparison between the single volume of QSM timeseries and the over-run average QSM for 2D EPI MBI and 3D EPI data. The average maps show decreased noise content and therefore higher quality.

Figure 29 shows the magnitude phase and images obtained by complex motion correction as well as the corresponding, directly MC magnitude image. The motion correction in complex space resulted in a visible signal dropout in the magnitude image (compare middle and right image in Figure 29) and the creation of open-ended fringe lines in the phase image. Since the quality of unwrapping and thereby also field maps would be decreased, the QSM analysis was not carried out.

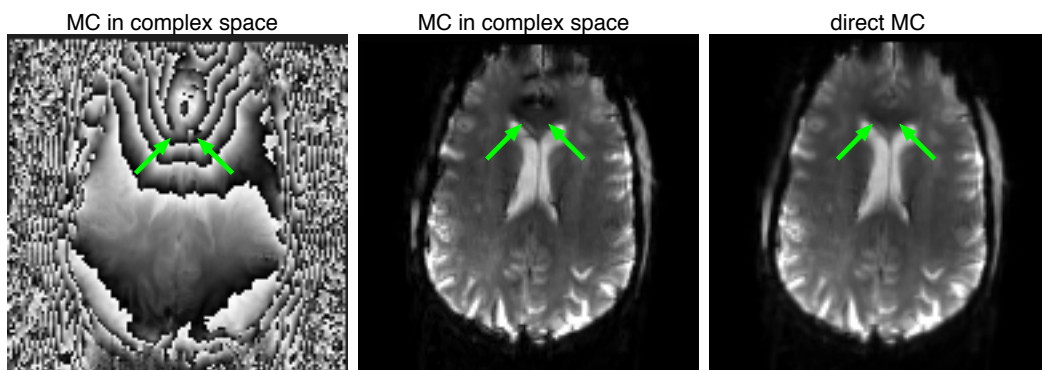


Figure 29: The results of motion correction in the complex space and the comparison with the directly MC magnitude image. Note the signal dropout and creation of open-ended fringe lines in the complex motion correction images.

6 Discussion

The aim of this thesis was to show the possibility of using the phase of task or resting state fMRI data for Quantitative Susceptibility Mapping and to observe the challenges and benefits of using conventional 2D EPI, 2D simultaneous multislice EPI or 3D EPI instead of the commonly used GRE. Further, an additional aim was to achieve the on-scanner high-quality phase combination of the EPI data by determination of the most suitable Virtual Receiver Coil image for the VRC approach and implementation of this approach in the Siemens Image Reconstruction Environment (ICE), making the use of time-series EPI for QSM a practical possibility in future studies.

Although the EPI data often show increased noise and overall decreased quality compared to slower sequences, using magnitude weighted SPM for VRC image creation together with the magnitude weighted combination of relative phase-offsets removed phase images of individual coils allowed for very high combination quality over the whole brain. The implementation of this method on the MR scanner allowed for fast, reliable phase combination without posing any special requirements on the measured data and greatly reduced the amount of the data that needs to be exported.

We have shown that the choice of measurement sequence and application of additional phase corrections may however greatly influence the quality of measured phase and should be taken into the consideration. When the 2D simultaneous-multi-slice EPI sequence developed at MGH with MB factor of 2 was used, the discontinuities in the upper halves of both single-channel and combined phase images were observed. We suspect that they were caused by the CAIPIRINHA shifting, resulting in the discontinuity between the blocks of regular and CAIPI-shifted slices and also between the individual CAIPI-shifted slices. To mitigate this artifact causing decreased combination quality, further studies of effects of different MB factors, slice interleaving and of special phase corrections would be required.

After the phase combination, the offline QSM analysis was carried out and the average susceptibility maps of all functional runs were compared with one of GRE scan. Because of the lower resolution of the measured EPI data and T_2^* blurring of the extended readout, the EPI QSMs were more blurry. Therefore, the fine structures such as small veins, microbleeds or calcifications may be obscured in EPI-QSM. Due to the long readout of 2D EPI sequence, the large susceptibility-differences at the air-tissue interface caused severe geometrical distortions and signal losses in the frontal regions, resulting in the cut-off susceptibility maps. To address this issue, the distortion correction algorithms

used in fMRI could be applied or, as we have showed in this study, the segmented 3D EPI sequence could be used. Although the 3D EPI data were more noisy, they provided higher signal intensity in those frontal regions. This was probably caused by the segmented sampling that reduced the time over which the signal decays and also by the fact that in 3D acquisition, N_{slices} times more k-space points contribute to each image voxel when compared with 2D. Further, also triggered by the long readout, the EPI phase contained more wraps and was more noisy, making it is more prone to unwrapping errors.

The EPI QSMs showed significant overestimation of susceptibility values in most of the ROIs and also to their larger variance over the ROIs, when compared with "gold standard" GRE QSM. These differences might have been caused by EPI's TE shifts, although that would be in the disagreement with the results of Sun et al. [3], who have not observed any significant differences. Another possible reason, as suggested in [87] [88], is the difference between resolutions of measured EPI and GRE data. Nevertheless, new contrast highly sensitive to the iron and myelin was achieved without the need of acquiring any additional data. Further, we have showed that by averaging QSMs calculated for each volume separately over the run, the QSM with decreased noise and hence increased quality can be obtained.

In contrast to the observations of Sood et al. [52], who reported the nonlinearities in the phase evolution caused by tissue anisotropy making the estimated susceptibility values dependent on the evolution time, in our study no significant effects of echo time on the mean susceptibilities over ROIs located in the deep grey matter structures estimated from GRE data were observed. This discrepancy might have been caused by the fact, that since we have used only two, relatively closely spaced TEs, we were not able to cover the very complicated relation between the susceptibility and echo time, which depends on the tissue cytoarchitecture and iron content and therefore is different for each region of interest. However, we observed that the longer phase evolution time of second echo of GRE allows for better venous contrast in QSMs, as previously showed by Koopmans et al. [89] and also for the reduced noise as reported by Liu et al. [90]. Since the echo time of EPI is often different than the one of GRE, and moreover since in multi-echo sequences such as EPI is the echo time inherently varies across k-space, the relation between the tissue anisotropy, used TE and estimated susceptibility should be studied in more detail.

No significant difference between the QSMs generated from the data combined by VRC that leaves arbitrary phase offset and by ASPIRE that removes the phase offset completely was observed. Since the phase offset introduced by VRC is generally very smooth, its influence can be suppressed by the background field removal. Common to that, the Laplacian unwrapping applied in TGV-based

QSM algorithm itself introduces some background field suppression, unless an exact solution is implemented. The susceptibility values were therefore not affected by the phase combination method, however if the VRC combined phase would be used without the background removal, biased results would be obtained.

Although the general fMRI analysis of magnitude data showed significant task-related changes in the activation of motoric and visual centers as well as in the resting state networks, no significant changes related to any of those activations were observed in the fQSM analysis. In previous studies [6] [11] [12] [13] [91], it was shown that the task-related changes in fQSM could be observed, however that the efficient spatial filtering for static background phase removal and temporal filtering for physiological noise removal are required, since the noise contribution to the phase instability is significant [9]. Nevertheless, in our study the changes in fQSM triggered by task-related activation were not observable neither after temporal filtering. In comparison to the similar studies, the resolution used here (3x3x3 mm) was quite low. Because of the orientation dependency of microscopic field perturbation the effects of BOLD changes on the phase signal are macroscopically averaging out and the substantial phase contrast can be found only near the veins with the diameter comparable to the voxel size. And since the susceptibility sources can be mapped only if their non-local phase effects are observed, the lower resolution might have caused the fQSM's detection rate decrease, as shown by Sun et al. [11]. The influence of BOLD-related susceptibility changes on the phase is thus very subtle and can be easily covered by a motion or by other physiological fluctuations. To observe the task-related fQSM changes, probably the improved statistics (more runs), higher resolution and enhanced physiological and other phase corrections would be necessary.

It was shown that the fQSM results are more likely to be affected by stimulus-independent physiological changes [9] [10]. In our study, a component localized mainly in the sagittal sinus with the main frequency that might correspond to the resting breathing rate (1 per 9 seconds) was observed. It is suspected to represent the changes related in blood flow, volume and oxygenation level that occur during breathing cycle. This component also contained harmonic frequencies that are often present in physiological signals [92]. However, for certain assessment, the measurement of respiration cycle with the belt sensor would be required.

No smoothing prior to the fQSM analysis was applied since the resolution of measured data was already quite low, however as showed by Balla et al. [6] the Gaussian smoothing significantly affects the susceptibility values of individual voxels and can be used to decrease the influence of thermal noise, thereby improving the statistical analysis for the price of decreased resolution.

The idea of calculating the average QSM of the EPI run by a single QSM analysis out of over-run average magnitude and phase is very appealing as the computational time would be decreased almost by the factor of a repetition number. However, as observed in this study, since the real and imaginary images on which the complex MC is performed contain high-intensity and low-intensity strikes (see Figure 12) similar to those of phase but less sharp, their averaging may lead to a complex signal cancelation. Therefore, this approach may result in a decreased quality of QSM analysis.

7 Conclusion

It has been shown that the optimized VRC approach can be used to perform high quality phase-combination of EPI data without the need for any additional MRI scans. By implementation of this approach on the Siemens MR scanner, we have allowed for significant reduction of data amount that needs to be exported making this analysis feasible. Further we have showed that the phase offset introduced by VRC approach does not influence the obtained susceptibility values.

We have achieved to perform QSM analysis using the reliably combined phase of 7T task and resting state fMRI data. However, the susceptibility values estimated from measured EPI data were significantly different from those of "gold standard" GRE and the functional QSM analysis did not show any task-related susceptibility changes. Since both of these problem might have been primarily caused by too low resolution of EPI data, in the continuing studies the effect of using higher resolution and of more advanced preprocessing methods for fQSM analysis will be evaluated.

Future we will involve the study of additional differences between EPI and GRE sequence, as for example the EPI inherent phase corrections, EPI's variability of echo time across k-space or additional phase shifts in parallel imaging acquisition, whose effects on QSM analysis need to be addressed, before the EPI-based QSMS could be reliably used.

References

- [1] Wen J, Cross AH, Yablonskiy DA. On the role of physiological fluctuations in quantitative gradient echo MRI: implications for GEPCI, QSM, and SWI. *Magn Reson Med* 2015;73:195-203.
- [2] Mansfield P. Multi-planar image formation using NMR spin echoes. *J Phys C: Solid State Phys* 1977;10:55-58.
- [3] Sun H, Wilman AH. Quantitative susceptibility mapping using single-shot echo-planar imaging. *Magn Reson Med* 2015;73(5):1932-1938.
- [4] Bilgic B, Gagoski BA, Cauley SF, Fan AP, Polimeni JR, Grant PE, Wald LL, Setsompop K. Wave-CAIPI for highly accelerated 3D imaging. *Magn Reson Med* 2015;73(6):2152-2162.
- [5] Langkammer C, Bredies K, Poser BA, Barth M, Reishofer G, Fan AP, Bilgic B, Fazekas F, Mainero C, Ropele S. Fast quantitative susceptibility mapping using 3D EPI and total generalized variation. *Neuroimage* 2015;111:622-630.
- [6] Balla DZ, Sanchez-Panchuelo RM, Wharton SJ, Hagberg GE, Scheffler K, Francis ST, Bowtell R. Functional quantitative susceptibility mapping (fQSM). *Neuroimage* 2014;100:112-24.
- [7] Deh K, Nguyen TD, Eskreis-Winkler S, Prince MR, Spincemaille P, Gauthier S, Kovanlikaya I, Zhang Y, Wang Y. Reproducibility of quantitative susceptibility mapping in the brain at two field strengths from two vendors. *Magn Reson Med* 2015;42(6):1592-1600.
- [8] Sun H, Seres P, Wilman AH. Structural and functional quantitative susceptibility mapping from standard fMRI studies. *NMR Biomed.* 2015;30:e3619.
- [9] Hagberg GE, Bianciardi M, Brainovich V, Cassara AM, Maraviglia B. Phase stability in fMRI time series: effect of noise regression, off-resonance correction and spatial filtering techniques. *Neuroimage* 2012;59:3748-3761.
- [10] Petridou N, Schafer A, Gowland P, Bowtell R. Phase vs. magnitude information in functional magnetic resonance imaging time series: toward understanding the noise. *Magn Reson Imaging* 2009;27,1046-1057.
- [11] Sun H, Seres P, Wilman AH. Structural and functional quantitative susceptibility mapping from standard fMRI studies. *NMR Biomed.* 2017;30:e3619.
- [12] Özbay PS, Deistung A, Feng X, Nanz D, Reichenbach JR, Schweser F. A comprehensive numerical analysis of background phase correction with V-SHARP. *NMR Biomed.* 2017;30:e3550.
- [13] Bianciardi M, van Gelderen P, Duyn JH. Investigation of BOLD fMRI resonance frequency shifts and quantitative susceptibility changes at 7 T. *Hum Brain Mapp.* 2014;35(5):2191–2205.
- [14] Parker DL, Payne A, Todd N, Hadley JR. Phase reconstruction from multiple coil data using a virtual reference coil. *Magn Reson Med* 2014;72(2):563-569.
- [15] Levitt MH. *Spin Dynamics: basics of nuclear magnetic resonance.* 2nd ed. Chichester, England: John Wiley & Sons, c2008, xxv, 714 p, ISBN 9780470511183.
- [16] Huettel SA, Song AW, McCarthy G. *Functional magnetic resonance imaging.* 2nd ed. Sunderland: Sinauer Associates, c2009, 542 p, ISBN 9780878932863.
- [17] Rabi II, Zacharias JR, Millman S, Kusch P. A new method of measuring nuclear magnetic moment. *Physical Review* 1938;53(4):318-327.
- [18] Bloch F, Hansen W, Packard M. Nuclear induction. *Physical Review.* 1946;70(7-8):460-474.
- [19] Ernst RR, Anderson WA. Application of Fourier transform spectroscopy to magnetic resonance. *Rev Sci Instrum* 1966;37:93-102.
- [20] Hornak JP. *The Basics of MRI.* 1996-2017. Available online: <<http://www.cis.rit.edu/htbooks/mri/>> [cit. 2017-05-10]
- [21] <http://www.lundorf.dk/mr4/Nyere%20pulssekvenser.htm> [cit. 2017-05-10]
- [22] <https://www.spl.harvard.edu/archive/spl-pre2007/pages/papers/zientara/fast/fastimaging.html> [cit. 2017-05-10]
- [23] Chen Q, Stock KW, Prasad PV, Hatabu H. Fast magnetic resonance imaging techniques, *EUR J Radiol.* 1999;29(2):90-100.
- [24] Deistung A, Schweser F, Reichenbach JR. Overview of quantitative susceptibility mapping. *NMR Biomed.* 2017;30:e3569.

- [25] Triantafyllou C, Hoge RD, Krueger G, Wiggins CJ, Potthast A, Wiggins GC, Wald LL. Comparison of physiological noise at 1.5 T, 3 T and 7 T and optimization of fMRI acquisition parameters, *Neuroimage* 2005;26(1):243-250.
- [26] Beisteiner R, Robinson S, Wurnig M, et al. Clinical fMRI: Evidence for a 7 T benefit over 3 T. *Neuroimage*. 2011;57(3):1015-1021.
- [27] Duyn JH, van Gelderen P, Li TQ, deZwart JA, Koretsky AP, Fukunaga M. High-field MRI of brain cortical substructure based on signal phase. *Proc Natl Acad Sci USA* 2007;104(28):11796–11801.
- [28] Haacke EM. Understanding Magnetic Resonance Imaging. *Magn Reson Med* 1999;41:855-856.
- [29] Roemer PB, Edelstein WA, Hayes CE, Souza SP, Mueller OM. The NMR phased array. *Magn Reson Med* 1990;16(2):192-225.
- [30] Li W, Wu B, Liu C. Quantitative susceptibility mapping of human brain reflects spatial variation in tissue composition. *Neuroimage* 2011;55:1645-1656.
- [31] Dymerska B, Poser BA, Barth M, Tractnig S, Robinson SD. A method for the dynamic correction of B0-related distortions in single-echo EPI at 7T. *Neuroimage* 2016
- [32] Jezzard P, Balaban RS. Correction for geometric distortion in echo planar images from B0 field variations. *Magn Reson Med* 1995;34(1):65-73.
- [33] Haacke EM, Xu Y, Cheng YC, Reichenbach JR. Susceptibility weighted imaging (SWI). *Magn Reson Med* 2004;52(3):612-618.
- [34] Liu C. Susceptibility tensor imaging. *Magn Reson Med* 2010;63(6):1471-1477.
- [35] Shmueli K, de Zwart JA, van Gelderen P, Li TQ, Dodd SJ, Duyn JH. Magnetic susceptibility mapping of brain tissue in vivo using MRI phase data. *Magn Reson Med* 2009; 62(6): 1510-1522.
- [36] Chavez S, Xiang QS, An L. Understanding phase maps in MRI: a new cutline phase unwrapping method. *IEEE Trans. Med. Imaging* 2002;21(8):966-977.
- [37] Robinson SD, Bredies K, Khabipova D, Dymerska B, Marques JP, Schweser F. An illustrated comparison of processing methods for MR phase imaging and QSM: combining array coil signals and phase unwrapping. *NMR Biomed*. 2017;30:e3601.
- [38] Robinson S, Grabner G, Witoszynskyj S, Tractnig S. Combining phase images from multi-channel RF coils using 3D phase offset maps derived from a dual-echo scan. *Magn Reson Med* 2011;65(6):1638-1648.
- [39] Schofield M, Zhu Y. Fast phase unwrapping algorithm for interferometric applications. *Opt Lett*. 2003;1:1194-1197.
- [40] Bagher-Ebadian H, Jiang Q, Ewing JR. A modified Fourier-based phase unwrapping algorithm with an application to MRI venography. *J Magn Reson Imaging*. 2008;27(3):649-652.
- [41] Schweser F, Deistung A, Reichenbach JR. Foundations of MRI phase imaging and processing for Quantitative Susceptibility Mapping (QSM). *Z. Med. Phys.* 2016;26:6-34.
- [42] Kaza E, Klose U, Lotze M. Comparison of a 32-channel with a 12-channel head coil: are there relevant improvements for functional imaging? *J Magn Reson Imaging* 2011;34:173-183.
- [43] Pruessmann K, Weiger M, Scheidegger M, Boesiger P. SENSE: sensitivity encoding for fast MRI. *Magn Reson Med* 1999;42(5):952-962.
- [44] Bollmann S, Robinson SD, O'Brien K, Vegh V, Janke A, Marstaller L, Reutens D, Barth M. The challenge of bias-free coil combination for quantitative susceptibility mapping at ultra-high field. *Magn Reson Med* 2017.
- [45] Robinson SD, Dymerska B, Bogner W, et al. Combining phase images from array coils using a short echo time reference scan (COMPOSER). *Magn Reson Med* 2017;77(1):318-327.
- [46] Eckstein K, Dymerska B, Bachrata B, Bogner W, Poljanc K, Tractnig S, Robinson S. Robust and computationally efficient combination of multi-channel phase data from multi-echo acquisitions (ASPIRE). In progress.
- [47] Walsh DO, Gmitro AF, Marcellin MW. Adaptive reconstruction of phased array MR imagery. *Magn Reson Med* 2000;43:682-690.
- [48] Hammond KE, Lupo JM, Xu D, Metcalf M, Kelley DA, Pelletier D, Chang SM, Mukherjee P, Vigneron DB, Nelson SJ. Development of a robust method for generating 7.0 T multichannel phase images of the brain with application to normal volunteers and patients with neurological diseases. *Neuroimage* 2008;39(4):1682-1692.
- [49] Schäfer A, Turner R. A general method for generating multichannel phase images without

- using a body coil. ISMRM Workshop Series 2008: High Field Systems and Applications: "What's Special about 7T+?", Rome. 2008.
- [50] Schweser F, A.M., Deistung A, Lehr BW, Sommer K, Reichenbach JR. Harmonic phase subtraction methods are prone to B1 background components. Proceedings of the 19th annual meeting of the ISMRM. 2011. Montreal.
 - [51] Buehrer M, Boesiger P, Kozerke S. Virtual body coil calibration for phased-array imaging. Proceedings of the 17th Annual Meeting of the ISMRM, Honolulu, 2009; no 3209.
 - [52] Sood S, Urriola J, Reutens D, O'Brien K, Bollmann S, Barth M, Vegh V. Echo time-dependent quantitative susceptibility mapping contains information on tissue properties. *Magn Reson Med* 2017;77:1946-1958.
 - [53] Wharton S, Bowtell R. Fiber orientation-dependent white matter contrast in gradient echo MRI. *Proc Natl Acad Sci USA* 2012;109(45):18559-18564.
 - [54] Liu T, Spincemaille P, de Rochefort L, Kressler B, Wang Y. Calculation of susceptibility through multiple orientation sampling (COSMOS): a method for conditioning the inverse problem from measured magnetic field map to susceptibility source image in MRI. *Magn Reson Med* 2009;61(1):196-204.
 - [55] Bredies K, Kunisch K, Pock T Total generalized variation. *SIAM J Imaging Sci* 2010;3(3):492-526.
 - [56] Knoll F, Bredies K, Pock T, Stollberger R. Second order total generalized variation (TGV) for MRI. *Magn Reson Med* 2011;65:480-491.
 - [57] Ogawa S, Tank DW, Menon R, Ellermann JM, Kim SG, Merkle H, Ugurbil K. Intrinsic signal changes accompanying sensory stimulation: functional brain mapping with magnetic resonance imaging. *Proc Natl Acad Sci USA* 1992;89(13):5951-5955.
 - [58] Kwong KK, Belliveau JW, Chesler DA, Goldberg IE, Weisskoff RM, Poncelet BP, Kennedy DN, Hoppel BE, Cohen MS, Turner R, et al. Dynamic magnetic resonance imaging of human brain activity during primary sensory stimulation. *Proc Natl Acad Sci USA* 1992;89(12):5675-5679.
 - [59] Ogawa S, Lee TM, Kay AR, Tank DW. Brain magnetic resonance imaging with contrast dependent on blood oxygenation. *Proc Natl Acad Sci USA* 1990;87:9868-9872.
 - [60] Ogawa S, Tank DW, Menon R, Ellermann JM, Kim SG, Merkle H, Ugurbil K. Intrinsic signal changes accompanying sensory stimulation: functional brain mapping with magnetic resonance imaging. *Proc Natl Acad Sci USA* 1992;89(13):5951-5955.
 - [61] Fox P, Raichle M, Mintun M, Dence C. Nonoxidative glucose consumption during focal physiologic neural activity. *Science* 1988;241:462-464.
 - [62] Leithner Ch, Royl G, Offenhauser N, Fuchtemeier M, Kohl-Bareis M, Villringer A, Dirnagl U, Lindauer U. Pharmacological uncoupling of activation induced increases in CBF and CMRO₂. *Journal of Cerebral Blood Flow & Metabolism* 2010;30:311-322.
 - [63] <https://www.brainmapping.org/MarkCohen/Papers/EPI-fMRI.html> [cit. 2017-05-10]
 - [64] Feinberg DA, Hale JD, Watts JC, Kaufman L, Mark A. Halving MR imaging time by conjugation: demonstration at 3.5 kG. *Radiology* 1986;161:527-531.
 - [65] Jesmanowicz A, Bandettini PA, Hyde JS. Single-shot half k-space high-resolution gradient-recalled EPI for fMRI at 3 tesla. *Magn Reson Med* 1998;40:754-762.
 - [66] Xu J, Moeller S, Auerbach EJ, et al. Evaluation of slice accelerations using multiband echo planar imaging at 3 Tesla. *NeuroImage*. 2013;83:10.1016.
 - [67] Griswold MA, Jakob PM, Heidemann RM, Nittka M, Jellus V, Wang J, Kiefer B, Haase A. Generalized autocalibrating partially parallel acquisitions (GRAPPA). *Magn Reson Med* 2002;47:1202-1210.
 - [68] Deshmane A, Gulani V, Griswold MA, Seiberlich N. Parallel MR Imaging. *Journal of magnetic resonance imaging : JMRI*. 2012;36(1):55-72.
 - [69] Nunes RG, Hajnal JV, Golay X, Larkman DJ. Simultaneous slice excitation and reconstruction for single shot EPI; ISMRM 14th Annual Meeting. ISMRM; 2006. p. 293.
 - [70] Setsompop K, Gagoski BA, Polimeni JR, Witzel T, Wedeen VJ, Wald LL. Blipped-Controlled Aliasing in Parallel Imaging (blipped-CAIPI) for simultaneous multi-slice EPI with reduced g-factor penalty. *Magn Reson Med* 2012;67(5):1210-1224.
 - [71] Feinberg DA, Setsompop K. Ultra-fast MRI of the human brain with simultaneous multi-slice imaging. *J Magn Reson*. 2013;229:90-100.
 - [72] Moeller S, Yacoub E, Olman CA, et al. Multiband Multislice GE-EPI at 7 Tesla, With 16-Fold Acceleration Using Partial Parallel Imaging With Application to High Spatial and Temporal Whole-Brain FMRI. *Magn Reson Med* 2010;63(5):1144-1153.
 - [73] Song AW, Wong EC, Hyde JS. Echo-volume imaging. *Magn Reson Med* 1994;32:668-671.

- [74] Poser BA, Koopmans PJ, Witzel T, Wald LL, Barth M. Three dimensional echo-planar imaging at 7 Tesla. *Neuroimage* 2010;51(1):261-266.
- [75] Neggers SFW, Hermans EJ, Ramsey NF. Enhanced sensitivity with fast three-dimensional blood-oxygen-level-dependent functional MRI: comparison of SENSE–PRESTO and 2D-EPI at 3 T. *NMR Biomed.* 2008;21:663-676.
- [76] Heid O. US6043651 A. 2000.
- [77] Feiweier T. US0234221 A1. 2011.
- [78] McKeown MJ, Sejnowski TJ. Independent component analysis of fMRI data: examining the assumptions. *Hum. Brain Mapping* 1998;6:368-372.
- [79] Penny W, Roberts S, Everson R. ICA: Model order selection and dynamic source models. In S. Roberts and R. Everson, editors, *Independent Component Analysis: Principle and Practice*, chapter 12. CUP, 2001.
- [80] Beckmann CF, Noble JA, Smith SM. Investigating the intrinsic dimensionality of FMRI data for ICA. In *Seventh Int. Conf. on Functional Mapping of the Human Brain*, 2001.
- [81] Beckmann CF, Smith SM. Probabilistic independent component analysis for functional magnetic resonance imaging. *IEEE Trans.Med.Imaging* 2004;23:137.
- [82] Robinson SD, Schopf V. ICA of fMRI Studies: New Approaches and Cutting Edge Applications. *Front Hum Neurosci* 2013;7:724.
- [83] Cox RW, Ashburner J, Breman H, Fissell K, Haselgrove C, Holmes CJ, Lancaster JL, Rex DE, Smith SM, Woodward JB, Strother SC. A (sort of) new image data format standard: NiFTI-1,”. 10th Annual Meeting of the Organization for Human Brain Mapping (OHBM 2004); Budapest. 2004.
- [84] Robinson SD, Siemens DICOM sort and convert to NifTI. 2008.
- [85] <http://fsl.fmrib.ox.ac.uk/fslcourse/lectures/practicals/melodic/>
- [86] Jenkinson M, Bannister P, Brady JM, Smith SM. Improved Optimisation for the Robust and Accurate Linear Registration and Motion Correction of Brain Images. *Neuroimage* 2002;17(2): 825-841.
- [87] Deistung A, Rauscher A, Sedlacik J, Stadler J, Witoszynskyj S, Reichenbach, JR. Susceptibility weighted imaging at ultra high magnetic field strengths: theoretical considerations and experimental results. *Magn Reson Med* 2008;60:1155-1168.
- [88] Haacke EM, Liu S, Buch S, Zheng W, Wu D, Ye Y. Quantitative susceptibility mapping: current status and future directions. *Magn Reson Imaging.* 2015;33:1-25.
- [89] Koopmans PJ, Manniesing R, Niessen WJ, Viergever MA, Barth M. MR venography of the human brain using susceptibility weighted imaging at very high field strength. *Magnetic Resonance Materials in Physics, Biology and Medicine* 2008;21:149-158.
- [90] Liu T, Surapaneni K, Lou M, Cheng L, Spincemaille P, Wang Y. Cerebral microbleeds: burden assessment by using quantitative susceptibility mapping. *Radiology* 2012;262(1):269-278.
- [91] Özbay PS, Rossi C, Warnock G, Kuhn F, Akin B, Prüssmann K, Nanz D. Independent component analysis (ICA) of functional QSM. *Proceedings of the 23rd Annual Meeting ISMRM, Toronto, 2015*, p. 3932.
- [92] Beissner F, Baudrexel S. Investigating the human brain stem with structural and functional MRI. Internet resource. *Frontiers Media SA, c2014, 92 p, ISBN 9782889192472*